Energy Bursts from the Fe_8 Molecular Magnet during Quantum Tunneling Of Magnetization Process.

Tom Leviant

Energy Bursts from the Fe_8 Molecular Magnet during Quantum Tunneling Of Magnetization Process

Research Thesis

In Partial Fulfillment of the
Requirements for the
Degree of Doctor of Philosophy

Tom Leviant

Submitted to the Senate of the Technion - Israel Institute of Technology
Elul 5774 HAIFA September 2014

"Perfection. That's what it's about. It's those moments. When you can feel the perfection of creation. The beauty of physics, you know, the wonder of mathematics. The elation of action and reaction, and that is the kind of perfection that I want to be connected to."

Sam Anders, Battlestar Galactica.

Abstract

Single molecule magnets (SMM) have been widely investigated as model compounds for quantum tunneling of magnetization. In the Fe_8 molecular magnet tunneling can occur from a meta-stable state to an excited state followed by a transition to the ground state. This transition is accompanied by an energy release of 115.6 GHz. Previous work done by Oren Shafir and Amit Keren [1] showed a jump in the temperature of a thermometer placed far from the sample, every time a tunneling event took place. The first objective of this research was to measure whether this energy is released in the form of thermal or electromagnetic energy. Contrary to a previous publication we find no evidence for the release of electromagnetic radiation. However, under some conditions this release of heat causes magnetization reversal in the form of a deflagration. The deflagration ignites by tunneling and its front velocity is of the order of 1 m/sec. This velocity is sensitive to field gradients and sweep rates. In addition, the propagation velocity of a heat pulse through the sample was measured. These measurements are discussed in the context of deflagration theory.

The Research Thesis Was Done Under The Supervision of Prof. Amit Keren
in the Faculty of Physics

Acknowledgements

I I I I I

I would like to express my deep appreciation and gratitude to my advisor Prof. Amit Keren, you have been a tremendous mentor for me. I would like to thank you for encouraging my research and for allowing me to grow as a researcher. Your guidance on both research as well as on my career have been priceless.

I would like to thank Prof. A. Kanigel, Prof. E. Polturak and Prof. M. Reznikov for their experienced help and advice in low temperature measurements.

Special thanks to my friends Gil and Tal for their endless support and friendship over the years.

I would like to thank William Livingstone for proofreading this thesis.

I would also like to thank my committee members, Prof. Yosef Yeshurun, Prof. Saar Rahav, Prof. Emil Polturak for serving as my committee and letting my defense be an enjoyable moment.

It is a pleasure to thank my parents, Galya and Yosef for all the support and encouragement.

At the end I would like to express appreciation to my beloved wife Ira who spent sleepless nights with me and was always my support.

The Generous Financial Help of the Technion is Gratefully Acknowledged

Contents

List of Figures

Abbreviations

2DEG	**2D E**lectorn **G**as
DR	**D**ilution **R**efrigerator
GE	**G**eneral **E**lectric
IVC	**I**nner **V**acuum **C**hamber
PCB	**P**rinted **C**ircuit **B**oard
SMM	**S**ingle **M**olecule **M**agnet
SNR	**S**ignal **N**oise **R**atio
SR	**S**uper **R**adiance
QTM	**Q**uantum **T**unneling of **M**agnetization
ZFS	**Z**ero **F**ield of **S**plitting

Chapter 1

Introduction

1.1 Single Molecule Magnets and Nano-Magnetism

Nano-magnetism is defined as the discipline dealing with magnetic structures of a sub-micron dimension. This area of research appears to provide a large number of novel applications, from high density magnetic media, to new types of devices where the charge property of the electron is combined with its spin (*i.e.* spintronics)[2, 3]. Magnetic molecules represent the ultimate possible size of a nano-magnet, providing a unique opportunity to observe the coexistence of classical and quantum properties. Single molecule magnets (SMM) consist of clusters of a finite number of magnetic centers (transition-metal or rare-earth ions, or even organic radicals) strongly coupled with each other, and surrounded by shells of ligand molecules. At low temperatures the resulting intra-cluster interactions exceed inter-cluster ones, such that every magnetic molecule can be considered a single (nano)-object with a high spin ground state ($S \approx 10$) and large zero field splitting. This means a large energy barrier between the spin-up and the spin-down states which leads to a relatively long relaxation time ($\approx 5 \times 10^5\ s$).

However, the molecules do interact with each other through magnetic dipolar interactions and the lattice (e.g. phonons). This research thesis investigates the influence of such intermolecular interactions on the energy released from an SMM when it decays from an excited state to the ground state. Usually these molecules are well ordered, forming crystals of macroscopic sizes. These materials are thus in between the macro and microscopic world, since macroscopic measurements can give access to the properties of the single molecule (ensemble average), which are governed by the laws of quantum

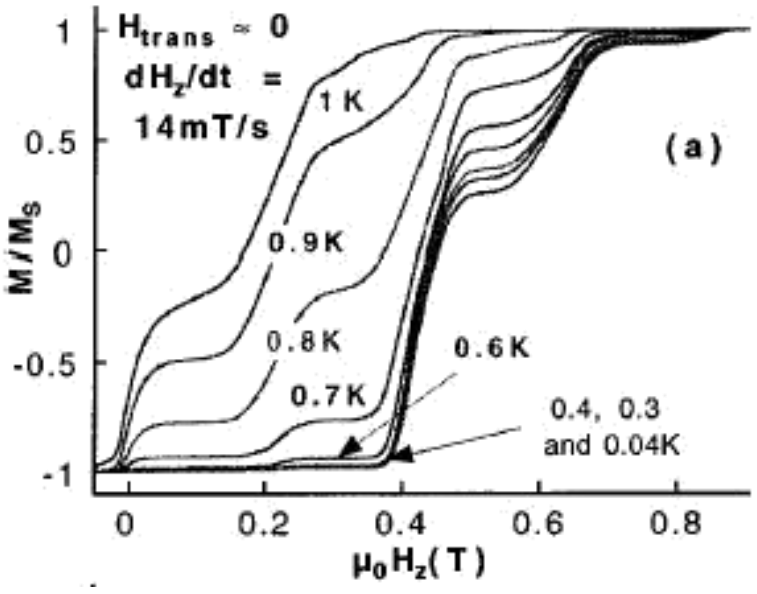

FIGURE 1.1: Temperature dependence of hysteresis loops [5]

mechanics. SMMs are to date the best candidates to observe quantum effects in magnets, such as the tunneling of the magnetization described in section 1.5, superradiance described in section 1.6 and the tunneling effect in magnetic deflagration described in section 1.7.

The single molecular magnet $[(C_6H_15N_3)_6Fe_8O_2(OH)_12]Br_7(H_2O)Br{\cdot}8H_2O$, abbreviated Fe_8, is a representative compound in which quantum tunneling of magnetization (QTM) has been observed, in the form of temperature-independent (below $T \approx 400$ mK), regularly-spaced steps (every ≈ 0.225 T) in the hysteresis loop [4–6] as seen in Figure 1.1 taken from Ref. [5]. Namely, it exhibits 'pure' quantum tunneling of the magnetization below 400 mK. These magnetization steps could be understood using only the spin Hamiltonian as described in section 1.2.

1.2 The Spin Hamiltonian

When a magnetic ion with d electrons is placed in a crystal field, the angular momentum is quenched and the only degree of freedom is the spin. When the spin-orbit interaction is taken into account, second order perturbation theory can lead to a coupling of a spin

with itself. At this order of the perturbation, the combined effect of the crystal-fields and spin-orbit interaction is a spin Hamiltonian of a quadratic form, given by [7]

$$\mathcal{H} = \mathbf{S} \cdot \mathbf{D} \cdot \mathbf{S} \tag{1.1}$$

where **D** is a real, symmetric tensor. The coordinate axes x, y, z can be chosen such that **D** is diagonal and 1.1 takes the form:

$$\mathcal{H}_0 = D_{xx}S_x^2 + D_{yy}S_y^2 + D_{zz}S_z^2 \tag{1.2}$$

where S_x, S_y, S_z are spin Operators.
After subtracting

$$(1/2)(D_{xx} + D_{yy})(S_x^2 + S_y^2 + S_z^2) = (1/2)(D_{xx} + D_{yy})S(S+1) \tag{1.3}$$

which is a constant and does not change the physical properties of the system.
We are left with:

$$\mathcal{H} = DS_z^2 + E \cdot \left(S_x^2 - S_y^2\right) \tag{1.4}$$

where:

$$D = D_{zz} - \frac{1}{2}D_{xx} - \frac{1}{2}D_{yy}; \quad E = \frac{1}{2}\left(D_{xx} - D_{yy}\right) \tag{1.5}$$

D can be positive or negative. If D is positive the levels with the lowest $|m|$ are the most stable and vice versa. Positive D corresponds to easy-plane magnetic anisotropy, negative D to easy-axis type magnetic anisotropy. Higher order spin terms are also possible and are given below.

It follows from equation 1.5 that in cubic symmetry D and E are equal to zero since $D_{xx} = D_{yy} = D_{zz}$ and in uniaxial symmetry only $E = 0$ since $D_{xx} = D_{yy} \neq D_{zz}$. Thus, in uniaxial symmetry, the $(2S+1)$ spin levels are expressed only with the D parameter. The energy barrier is present even in the absence of an applied external magnetic field. Therefore this effect is often called zero-field splitting (ZFS). The E parameter mixes the m_s states, i.e. the pure m_s states are no longer the energy Eigenstates of the system and tunneling between them can take place. Thus, E is responsible for the tunnel splitting. In the next section we examine the spin Hamiltonian of the Fe_8 compound.

1.3 Fe_8 Compound

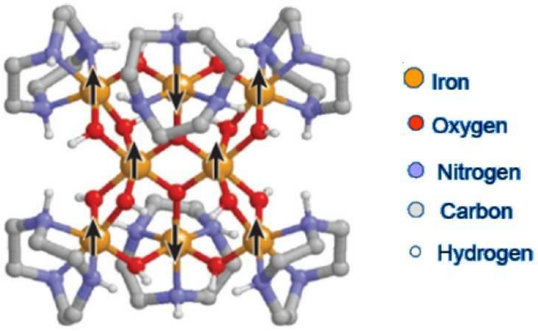

FIGURE 1.2: Schematic structure of Fe_8 with the suggested preferred orientation of the individual spins. [8]

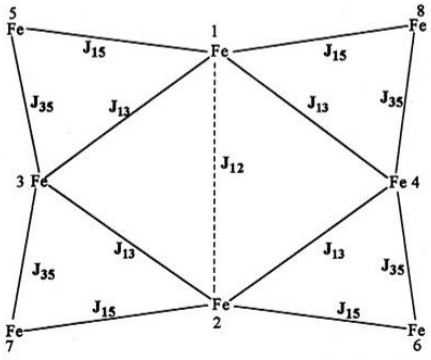

FIGURE 1.3: Scheme of the exchange pathways connecting iron (III) centers in Fe_8

The Fe_8 compound, seen in Figure 1.2, was first reported by Wieghardt in the 1980s [9]. It meets the conditions for behaving as a SMM. The antiferromagnetic interactions between the spins of the ions are in the range of 20 to 170K, as seen in Figure 1.3 and in the table below[10]:

J_{12}(K)	J_{13}(K)	J_{15}(K)	J_{35}(K)
-147	-173	-22	-50

At temperatures below the magnetic coupling between ions inside the molecule, the spins of the ions are locked and the molecule shows an $S = 10$ ground state with an Ising type magnetic anisotropy [11]. The temperature dependence of χT indicates a ferromagnetic behavior with a ground $S = 10$ state confirmed by high-field magnetization measurements [10]. This ground state can be justified by putting six ($S = \frac{5}{2}$) spins up and two down. The fit of the temperature dependence of the susceptibility, and polarized neutrons diffraction experiment [12] suggest that the spin arrangement is as shown by the arrows in Figure 1.2. The ground $S = 10$ state has a large zero-field splitting and relatively small tunnel splitting that has been measured by HF-EPR (High Field Electron Paramagnetic Resonance) [11, 13], inelastic neutron scattering,[14, 15] and far infrared spectroscopy[16]. The results are concentrated in the table below:

$$\mathcal{H} = DS_z^2 + E\left(S_x^2 - S_y^2\right) + B_4^0 O_4^0 + B_4^2 O_4^2 + B_4^4 O_4^4 \tag{1.6}$$

D(K)	$\lvert E/D\rvert$	B_4^0(K)	B_4^2(K)	B_4^4(K)	Ref
-0.295	0.19	2.3×10^{-6}	-7.2×10^{-6}	-1.2×10^{-5}	[13]
-0.292	0.16	1.0×10^{-6}	1.2×10^{-7}	8.6×10^{-6}	[14]
-0.295	0.15	2.0×10^{-6}	1.2×10^{-7}	8.6×10^{-6}	[16]

where:

$$\begin{aligned} O_4^2 &= \tfrac{1}{4}\left\{\left[7S_z^2 - S\left(S+1\right) - 5\right]\left(S_+^2 + S_-^2\right) + \left(S_+^2 + S_-^2\right)\left[7S_z^4 - S\left(S+1\right) - 5\right]\right\} \\ O_4^3 &= \tfrac{1}{4}\left[S_z\left(S_+^3 + S_-^3\right) + \left(S_+^3 + S_-^3\right)S_z\right] \\ O_4^4 &= \tfrac{1}{2}\left(S_+^4 + S_-^4\right) \end{aligned} \tag{1.7}$$

Also, the magnetic interactions between the molecules are negligibly small as compared to the zero field splitting ($\approx 0.05\ K$), and the molecules on the lattice should behave like non-interacting spins. However, in reality, to fully understand the magnetization steps, one must introduce terms linear in S_+ and S_- despite the fact that they are not allowed by the crystal symmetry. This suggests that intermolecular interaction or nuclear moments could not be completely neglected in the model for quantum tunneling of magnetization (QTM).

1.4 Thermal Relaxation in Molecular Magnets

At non zero temperature when neglecting tunneling effect, the population of spins in the states $|m_i\rangle$ having an energy of E_i follows a Boltzman distribution and is proportional to $\exp\left(-\frac{E_i}{k_B T}\right)$. Then the population of state $|m_i\rangle$ is given by:

$$\begin{aligned} n_i &= \tfrac{1}{Z}\exp\left(-\tfrac{E_i}{k_B T}\right) \\ Z &= \sum_j \exp\left(-\tfrac{E_j}{k_B T}\right) \end{aligned} \tag{1.8}$$

The magnetization along the $\hat{z}$ direction is the sum of the population multiplied by the corresponding spin projections:

$$M_z = \sum_i n_i m_i \tag{1.9}$$

The dynamics of the magnetization can be described by equations for the number of spins in the left n_+ and right wells n_- of the potential:

$$\dot{n}_\pm = \pm\Gamma_- n_+ \mp \Gamma_+ n_- = \Gamma\left(n_\pm^{eq} - n_\pm\right). \tag{1.10}$$

where $\Gamma_\pm$ are the escape rates from the positive/negative wells and are described by the following equations:

$$\begin{aligned} \Gamma_- &= \Gamma_0 \exp\left(-\tfrac{U}{k_B T}\right) \\ \Gamma_+ &= \Gamma_0 \exp\left(-\tfrac{U+\Delta E}{k_B T}\right) \end{aligned} \tag{1.11}$$

where U is the energy barrier, ΔE the energy difference between the two wells and Γ_0 is the attempt frequency. Neglecting resonant tunneling, and using $\Gamma = \Gamma_+ + \Gamma_-$ we get a total relaxation rate of:

$$\Gamma = \Gamma_0 \exp\left[-\frac{U}{k_B T}\right]\left(1 + \exp\left[-\frac{\Delta E}{k_B T}\right]\right) \tag{1.12}$$

At high temperatures the spins are thermally activated and decay from one side of the well to the other in a time that is much shorter than the measuring times. The magnetic moments are in thermal equilibrium and $M_z \propto \frac{1}{T}$. At low temperatures, $k_B T \ll U$, the spins do not have enough energy to overcome the double well potential energy barrier. The system shows a slow relaxation and is practicliy metastable. When the time scale of spin relaxation becomes longer than the measuring time, $t_{measure}$, hysteresis loop will be observed in the magnetization curve due to "blocking" of the spins in one side of the well. The blocking temperature, T_B, is defined as the temperature below which the SMM shows hysteretic behavior. Solving $t_{measure} = \frac{1}{\Gamma}$, we get the blocking temperature:

$$T_B = \frac{U}{k_B \ln\left(\Gamma_0 t_{measure}\right)}. \tag{1.13}$$

In addition to classical thermal relaxation, at low temperatures tunneling between spin states must be taken into account.

1.5 Quantum tunneling of magnetization

1.5.1 Tunnel Splitting for S=1

To understand how quantum tunneling of the magnetization works, let us first assume for simplicity spin $S = 1$ and the Hamiltonian from equation 1.4. In matrix notation the Crystal Field Hamiltonian is given by:

$$\mathcal{H} = DS_z^2 + E \cdot \left(S_x^2 - S_y^2\right) = \begin{pmatrix} D & 0 & E \\ 0 & 0 & 0 \\ E & 0 & D \end{pmatrix}. \tag{1.14}$$

When $E = 0$ we get three eigenstates:

$$|up\rangle = \begin{pmatrix} 1 \\ 0 \\ 0 \end{pmatrix}, |middle\rangle = \begin{pmatrix} 0 \\ 1 \\ 0 \end{pmatrix} and\, |down\rangle = \begin{pmatrix} 0 \\ 0 \\ 1 \end{pmatrix} \tag{1.15}$$

If D is negative we have a double degenerate ground state with energy D and excited state with zero energy. When $E \neq 0$ the two states are coupled and the eigenvectors become:

$$\frac{1}{\sqrt{2}} \begin{pmatrix} 1 \\ 0 \\ -1 \end{pmatrix}, \frac{1}{\sqrt{2}} \begin{pmatrix} 1 \\ 0 \\ 1 \end{pmatrix} and \begin{pmatrix} 0 \\ 1 \\ 0 \end{pmatrix} \tag{1.16}$$

with eigenvalues: $(D - E)$, $(D + E)$ and 0 respectively. Since $|up\rangle$ and $|down\rangle$ are no longer eigenstates there is a probability to tunnel between them which is given by:

$$\left|\langle down| \exp\left(\frac{-i\mathcal{H}t}{\hbar}\right)|up\rangle\right|^2 = \frac{1 - \cos\left(2Et/\hbar\right)}{2} = \frac{1 - \cos\left(\Delta t/\hbar\right)}{2} \tag{1.17}$$

This means that the system will oscillate between the two states at a frequency of $2E/\hbar = \Delta/\hbar$ where $\Delta = 2E$ is called the Tunnel Splitting, and is illustrated in Figure 1.4. In order to observe the tunneling process one needs to prepare the system where all the spins are in one side of the double potential well.

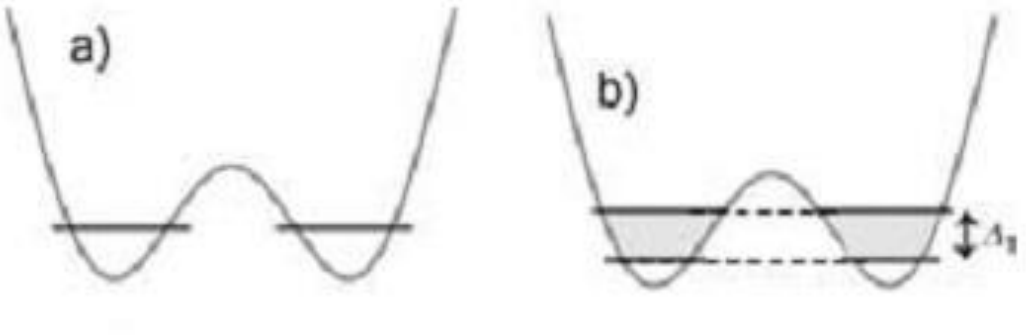

FIGURE 1.4: Tunneling in a double well system. a) Noninteracting states; b) interacting states giving rise to tunnel splitting Δ_t [17]

1.5.2 Quantum Tunneling for S=10

Now we look at the Fe_8 system with a well defined ground spin state, characterized by a large value of $S = 10$ and an external magnetic field parallel to the easy axis of the molecules. Adding the Ziman term and assuming $E = 0$ the Hamiltonian from Eq 1.4 can be written as:

$$\mathcal{H} = DS_z^2 - g\mu_B H_z S_z. \tag{1.18}$$

The energies are calculated to be:

$$E(M_s) = DM_s^2 + g\mu_B M_s H_z \tag{1.19}$$

where $-S \leq M_s \leq S$.

The energy levels can be illustrated as a double potential well as shown in Figure 1.5. When no external field is applied all the levels are double degenerate, except $M_s = 0$. Since D is negative, the $M_s = \pm S$ levels are the ground state. The states with positive M_s are plotted on one side of the barrier, and those with negative M_s on the other. The system can be prepared in a magnetized state by applying a strong magnetic field parallel to the easy axis. At low temperatures and positive field H_z, the $M_s = -10$ state will be the only one populated.

At low temperatures, where no phonons are available, only the degenerate $M_s = \pm 10$ levels will be populated. As long as $E = 0$ in the Hamiltonian of Eq 1.4, the two states

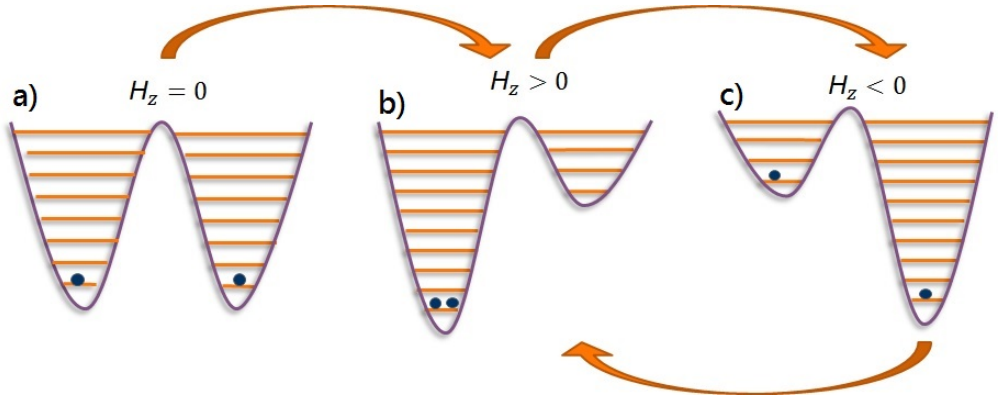

FIGURE 1.5: Energy levels for a spin state S with easy axis magnetic anisotropy. The +M levels are localized on the left side and the -M levels on the right side. a) In zero field the two states are equally populated; b) the application of a magnetic field selectively populates the left side; c) reversing the field direction populates the other side of the well

are orthogonal to each other, and there is no possibility of tunneling. In principle, since the two states are degenerate, all their linear combinations will be eigenfunctions of the system. To observe tunneling the two functions must be admixed by some suitable perturbation $\mathcal{H}_1$. It is the $\mathcal{H}_1 = E(S_x^2 - S_y^2)$ of Eq 1.4 that produces this admixing. And, as mentioned before, other terms such as disorder, distortion which removes the uniaxial symmetry, and molecular coupling can also contribute to the admixing.

The Hamiltonian $\mathcal{H}_1$ does not commute with $\mathcal{H}_0 = D(S_z^2)$, and therefore the eigenstates of the full Hamiltonian $\mathcal{H} = \mathcal{H}_0 + \mathcal{H}_1$ are an admixture of $|M_s\rangle$ states, with a different sign of M_s. The wavefunction is therefore partially delocalized on both wells and this may give rise to tunneling, which may occur not only between the lowest-lying states $M_s = \pm S$, but also between pairs of degenerate excited states. The fields at which crossing occurs, assuming $E << D$, are given by Eq 1.20:

$$H_m\,(n) = \frac{nD}{g\mu_B} \cong n \times 0.225\,[T] \tag{1.20}$$

Here H_m is called the "matching" fields since, at these fields, spin states with opposite signs have identical energies and tunneling can occur. The full energy diagram obtained by numerical diagonalization of the Hamiltonian is depicted in Figure 1.6. H_m represents fields at which lines cross each other (level crossing). With the reintroduction of E, the level crossing turns into an avoided crossing with a gap Δ, which is the tunnel splitting, as presented in the inset of Figure 1.6. Since $\mathcal{H}_1$ couples states with $|M_s - M_s'| = 2$

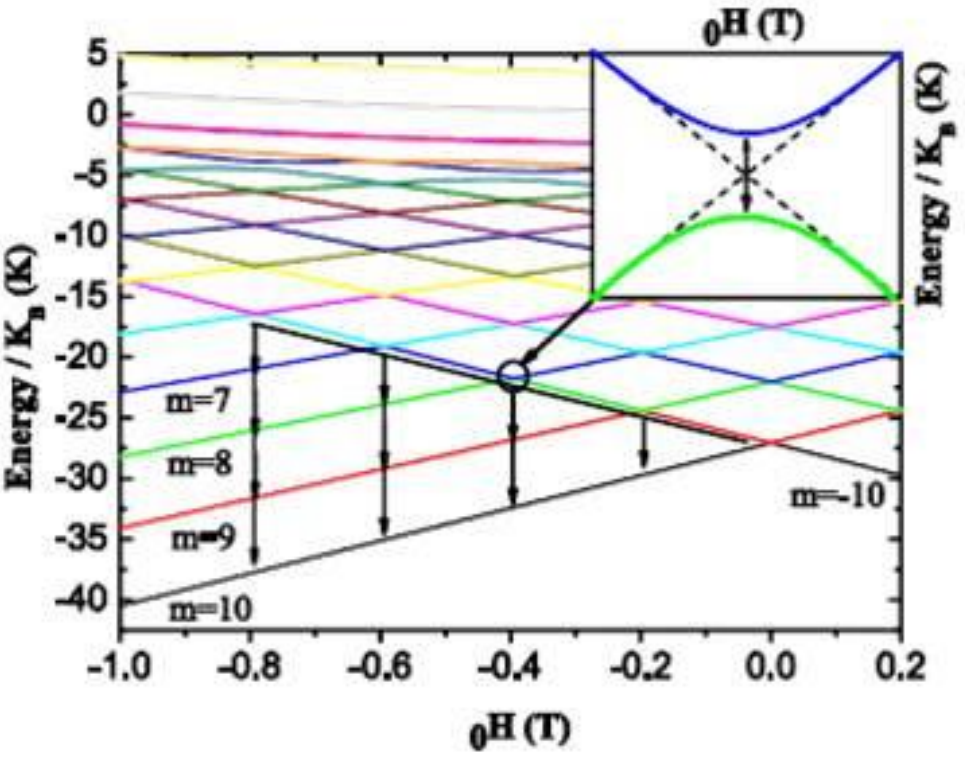

FIGURE 1.6: Zeeman diagram of the 21 levels of the S = 10 manifold of Fe_8 as a function of the magnetic field applied along the easy axis and the quantum numbers M_s . The inset is a zoom on the level crossing, which, in fact, is an avoided crossing with energy splitting [5]

(because $S_\pm = S_x \pm iS_y$) when sweeping the field from positive to negative, the tunneling that has the highest probability is taking place at $\mu_0 H \cong 0.44$ T meaning that the molecule tunnels from M_s=10 to M_s=-8, followed by a transition from M_s=-8 to M_s=-9 to M_s=-10, as illustrated by arrows in Figure 1.6.

The energy difference between two M_s states when $|M_s - M_s'| = n$ is given by:

$$\begin{aligned} \Delta E\,(n) &= 2n\,(S-n)\,D \\ \Delta E\,(n=1) &= 5.256\ Kelvin \\ \Delta E\,(n=2) &= 9.344\ Kelvin \end{aligned} \tag{1.21}$$

This energy can be released as thermal energy of radiation. If the energy releases as radiation, the frequencies are 109.5 Ghz for $M_s = -9$ to $M_s = -10$ transition and 85.2 Ghz for M_s=-8 to M_s=-9 transition. The wavelengths are $\approx 2.7\ mm$ and $\approx 3.5\ mm$ accordingly. As will be shown later, our sample size is also about $3 \times 3 \times 1\ mm^3$. This is

the elementary condition for Dicke Superradiance reviewed in section 1.6. If the energy is released as heat, it leads to a local temperature rise of $\Delta T = \Delta E/C_{ph}$ where C_{ph} is the phonon heat capacity per magnetic molecule. The higher temperature raises the transition probabilities and can cause magnetic deflagration which is discussed in section 1.7.

1.6 Superradiance (SR) - The Dicke model

Cooperative effects such as *Superradiance* and *Subradiance* are fundamental effects which originate from collective interactions of initially independent systems with the radiation field. When the molecules are confined to a volume smaller than radiation wavelength cubed, the spontaneous emission is enhanced when the molecules' dipole moments are in phase (superradiance) and inhibited when they are out of phase (subradiance). The first model for superadiance was suggested by Dicke in 1954 [18].

The Dicke model suggested a system with N atoms. First we discuss this model for two atoms only. Each atom is modeled as a two-level system with an energy difference of:

$$\Delta \mathrm{E} = \hbar\omega = \mathrm{hc}/\lambda \tag{1.22}$$

The non interacting states are:

$$|g_1 g_2\rangle \quad |g_1 e_2\rangle \quad |e_1 g_2\rangle \quad |e_1 e_2\rangle \tag{1.23}$$

where g_i and e_i are the ground and the excited state respectively. They can be represented as spin $\frac{1}{2}$ states and we can form *Dicke* states as a singlet:

$$|0,0\rangle = \frac{1}{\sqrt{2}}\left(|e_1 g_2\rangle - |g_1 e_2\rangle\right) \tag{1.24}$$

and triplet:

$$\begin{aligned} |1,1\rangle &= |e_1 e_2\rangle \\ |1,0\rangle &= \tfrac{1}{\sqrt{2}}\left(|e_1 g_2\rangle + |g_1 e_2\rangle\right) \\ |1,-1\rangle &= |g_1 g_2\rangle \end{aligned} \tag{1.25}$$

The $M = 0$ of the triplet and the singlet states both correspond to one excited atom and one at the ground state when $|1,0\rangle$ is the symmetric and $|0,0\rangle$ is the anti-symmetric state under atom exchange.

For a ensemble of N identical non-degenerate atoms Dicke defined collective spin operators:

$$\Delta_1 \equiv \sum_{j=1}^{N} \sigma_1^j \quad \Delta_2 \equiv \sum_{j=1}^{N} \sigma_2^j \quad \Delta_3 \equiv \sum_{j=1}^{N} \sigma_3^j \quad \Delta^2 \equiv \sum_{i=1}^{3} \Delta_i^2 \tag{1.26}$$

where $\sigma_{1,2,3}$ are the well known spin operators for a single atom which now work on the ground-excited Hilbert space.

The collective *Dicke* states are $\psi = |L, M\rangle$ where:

$$\Delta_3 |L, M\rangle = M |L, M\rangle$$

and

$$\Delta^2 |L, M\rangle = L(L+1) |L, M\rangle$$

with $|M| \leq L \leq \frac{N}{2}$.
The raising and lowering operators are:

$$\begin{aligned} \Delta^- |LM\rangle &= \sqrt{(L+M)(L-M+1)}\, |L, M-1\rangle \\ \Delta^+ |LM\rangle &= \sqrt{(L-M)(L+M+1)}\, |L, M+1\rangle . \end{aligned} \tag{1.27}$$

If the atoms are confined to a volume much smaller than the radiation wavelength cubed, λ^3 from Eq 1.22, the long wavelength approximation can be used. Meaning the electric field can be taken as a constant in space. Then the interaction Hamiltonian between the atoms and radiation can be written as:

$$V = e \sum_i \mathbf{E} \cdot \mathbf{r}_i \tag{1.28}$$

Using the Wigner-Eckart theorem

$r_i \propto \sigma_i$ with proportionality constant that is independent of i. Therefore,

$$V = const \cdot \mathbf{E} \cdot \mathbf{\Delta}. \tag{1.29}$$

This can be written as

$$V = \left(\vec{E}^{+}(0) + \vec{E}^{-}(0)\right) \cdot \left(\vec{d}_{ge}\Delta^{-} + \vec{d}_{eg}\Delta^{+}\right) \tag{1.30}$$

where $\vec{d}_{ge} = \langle g|\,\vec{d}\,|e\rangle$ and $\vec{d}_{eg} = \langle e|\,\vec{d}\,|g\rangle$ are electric dipole matrix elements of a single atom with $\vec{d} = q\vec{r}$ and:

$$\vec{E}^{+}(0) = i\sum_{\vec{k}\,\varepsilon}\sqrt{\frac{\hbar\omega_k}{2\varepsilon_0\Omega}}a_{\vec{k}\,\varepsilon}\,\hat{\varepsilon}_{\vec{k}} \quad \vec{E}^{-}(0) = \left[\vec{E}^{+}(0)\right]^{\dagger} \tag{1.31}$$

.

Calculating the transition rate from initial state, n_γ representing the number of photons, $i = |L, M, n_\gamma = 0\rangle$ to a final state with one emitted photon $f = |L, M \pm 1, n_\gamma = 1\rangle$, and leaving only the emission part of the Hamiltonian, we get:

$$\Gamma \propto \sum_{f}\left|\langle f|\left(\vec{d}_{ge}\cdot\vec{E}^{-}(0)\right)\Delta^{-}|i\rangle\right|^2 \tag{1.32}$$

Expression 1.32 can be written as:

$$\Gamma = \Gamma_0\,\langle LM|\,\Delta^{+}\Delta^{-}\,|LM\rangle \tag{1.33}$$

where Γ_0 is the single atom emission rate.

This finally yields:

$$\Gamma = (L+M)(L-M+1)\Gamma_0 \tag{1.34}$$

If all atoms are excited, meaning: $|L, M\rangle = \left|{}^{N}/_{2}, {}^{N}/_{2}\right\rangle$ then

$$\Gamma = N\Gamma_0 \tag{1.35}$$

which corresponds to N independent radiating atoms. If half of the atoms are excited, then: $|L, M\rangle = |L, 0\rangle$ and the emission rate is given by:

$$\Gamma = L\,(L+1)\,\Gamma_0 \tag{1.36}$$

where $0 \leq L \leq {}^{N}/_{2}$, L is called the *Cooperation number*. If L is at maximum, we get an enhancement of the spontaneous emission by approximately a factor of N:

$$L = {}^{N}/_{2} \quad \Rightarrow \Gamma = \frac{N}{2}\left(\frac{N}{2}+1\right)\Gamma_0 \qquad N >> 1 \Rightarrow \Gamma = \frac{N^2}{4}\Gamma_0 \tag{1.37}$$

This effect is called **Superradiance**. In the case of $L = 0$ we get $\Gamma = 0$ although half of the atoms are excited, this effect is called **Subradiance**.

In the example of two atoms the decay from the $|1,0\rangle$ to the ground state corresponds to the superradiating state with $\Gamma = 2\Gamma_0$ and the decay from the $|0,0\rangle$ to the ground state corresponds to the Subradiance with $\Gamma = 0$.

In molecular magnets one can control the number of spins (this time real magnetic spins) in the ground and excited states using different sweep rates. Therefore, it might be possible to prepare different Dicke states and study their influence on the radiation.

1.7 Magnetic Deflagration

Magnetic avalanche was first reported by Paulsen and Park [19]. Most of the work on this subject has been focused on Mn_{12}. Indeed, in Mn_{12} intriguing effects were found, such as deflagration [20, 21], quantum assisted deflagration [22], and detonation [23, 24]. In all these cases, a spin reversal front propagates through the sample in a form of deflagration. When the spins decay to the ground state and release their energy in the form of phonons, this leads to a rise in temperature of the neighboring molecules. In most cases the decay rate has the Arrhenius temperature dependence:

$$\Gamma = \Gamma_0 \exp\left[-\frac{U}{k_B T}\right]. \tag{1.38}$$

When the rate of the heat release exceeds the rate at which it defuses away from the neighbor sites, the temperature rises. This temperature rise increases the transition rates of the neighboring molecules, then more molecules decay and release more phonons. The relaxation becomes a self-sustained process with a hot front propagating through the sample at a constant velocity. This process can be described as magnetic deflagration when the Zeeman energy plays the role of chemical energy and the uniaxial anisotropy barrier is the activation energy, as seen in Figure 1.7. Contrary to regular deflagration, the burned area, *i.e.* the parts of the crystal with a spin parallel to the field, can be returned to a metastable state, in other words turn back to fuel simply by reversing the direction of the magnetic field. Hence, magnetic deflagration is non-destructive process and allows studies which are not possible with chemical deflagration. It is interesting

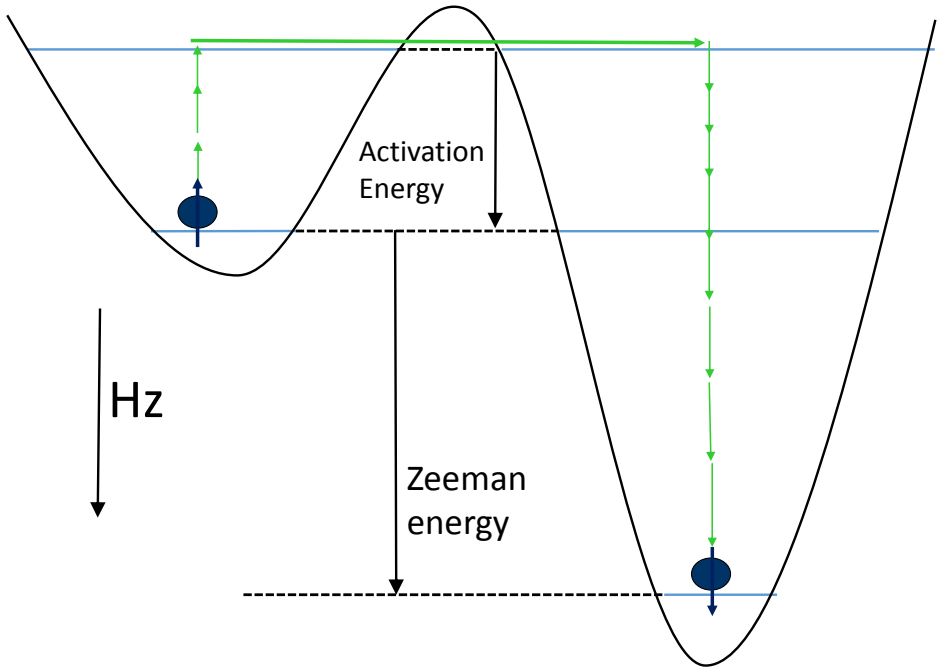

FIGURE 1.7: Activation and Zeeman energy in the deflagration process.

to notice that deflagration do not occur in traditional magnetic systems, even though many of them have a strong uniaxial anisotropy. In those materials the released energy is much smaller than in the case of a regular (chemical) deflagration. Meaning that in room temperatures, the temperature increase due to Zeeman energy is too small to change the relaxation rate and support deflagration. Only at low temperatures does the increase of the relaxation rate become large enough.

Magnetic deflagration theory is covered comprehensively in Ref. [25]. It includes calculations of the velocity of the burning front and ignition time due to local increase of temperature or change of the magnetic field. However, up to now there has been no good agreement between the theory and experiment for several reasons. First, the thermal diffusivity κ, which plays a critical role in the theory of deflagration has not yet been measured. Second, the theory does not take into account effects such as superradiance and phonon bottleneck.

The molecular magnets are famous for their quantum effects such as tunneling. The first discovery of magnetic avalanches [19] started the quest to link the classical effect

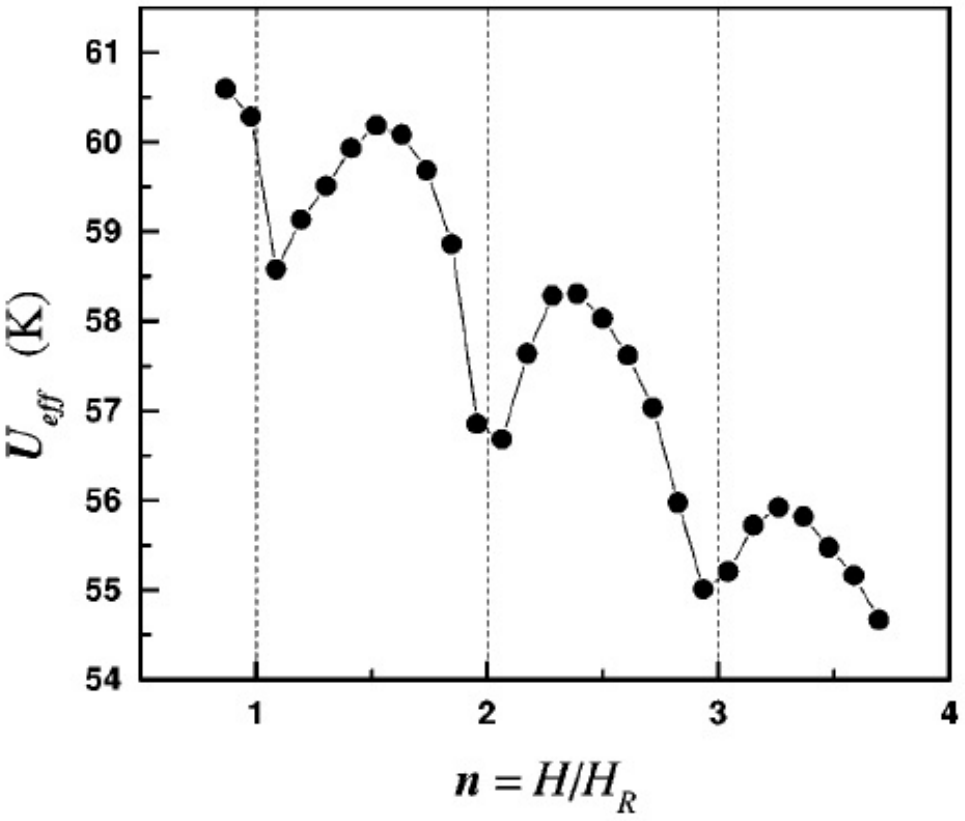

FIGURE 1.8: Effective barrier vs applied field H, obtained from the relaxation measurements . $H_R = 0.46T$ is the interval between resonant fields in Mn_{12}.

of deflagration to quantum phenomena of QTM. The simplest theory of magnetic deflagration [22, 25] describes the thermally assisted tunneling as an effective lowering of the energy barrier at the resonance values of the external field as seen in Figure.1.8 which has been taken from Ref.[26].

Further theoretical research led to the idea that the dipole-dipole interaction can play an active role in deflagration. By adding the dipole field to the external bias field, the dipolar field can set some molecules on or off resonance. And tunneling of one magnetic molecule changes the dipolar fields on the other ones, thus controlling the relaxation rate, as temperature does in thermal deflagration. A solution of this problem at zero temperature in the form of a moving front of tunneling has been calculated numerically [27] and analytically [28]. This effect is sometimes called cold deflagration.

1.7.1 Theory of Magnetic deflagration

The generic Hamiltonian for a molecular magnet

$$\mathcal{H} = DS_z^2 - g\mu_B H_z S_z + \mathcal{H}'. \tag{1.39}$$

where $\mathcal{H}'$ includes all the terms that do not commute with S_z and are responsible for the tunneling. We can define the energy barrier

$$U = (1-h)^2 U_0, \quad U_0 = DS^2, \quad h \equiv \frac{g\mu_B B_z}{2DS}. \tag{1.40}$$

The average energy per molecule released when decaying to the ground state given by

$$\Delta E = 2g\mu_B H_z S \left(\frac{\Delta M}{2M_s}\right) \tag{1.41}$$

where M_s is the saturation magnetization and ΔM is the change from initial to final state. The ignition of the deflagration is controlled by two processes: 1. the creation of heat given by

$$\Delta T = \Delta E / C \tag{1.42}$$

where C is the heat capacity per magnetic molecule. This is mainly due to phonons, whereas the magnetic contribution is relatively small. Then, 2. the diffusion of heat is given by the heat equation:

$$\frac{\partial T}{\partial t} = \frac{1}{C}\nabla \cdot k\nabla T - \frac{\Delta E}{C}\frac{dn}{dt} \tag{1.43}$$

where k is the heat conductivity. Neglecting the contribution of spin tunneling at low temperatures where $U/k_B T \ll 1$, the metastable population n is given by

$$\frac{dn}{dt} = -\Gamma\left(n - n^{eq}\right) \tag{1.44}$$

where Γ is the relaxation rate. From section 1.4 the equilibrium metastable population n^{eq} is given by

$$n^{eq} = \frac{1}{1 + \exp\left(\frac{\Delta E}{k_B T}\right)} \tag{1.45}$$

Assuming only phonon contribution, we can use the relation $C = d\epsilon/dT$ and rewrite equation 1.43 in terms of energy

$$\dot{\varepsilon} = \nabla \cdot \kappa \nabla \varepsilon - \dot{n} \Delta E. \tag{1.46}$$

where $\kappa = k/C$ it the thermal diffusivity which can be highly temperature-dependent at low temperatures.

Equations 1.12 , 1.44 , 1.46 with the relation

$$\varepsilon(T) = \int_0^T C\left(T'\right) dT' \tag{1.47}$$

are a very nonlinear set of equations. Although they can be solved numerically, finding an analytical solution is not an easy task.

1.7.2 Ignition of Deflagration

If the diffusion of heat is enough to keep the sample at a stationary low temperatures the deflagration will not ignite. In the other case, the heat loss through the boundaries is insufficient to compensate for the creation of heat by the decaying molecules. This will lead to the ignition of a self sustained deflagration process. For a cylindrical sample, the condition for ignition is met when the relaxation rate is higher than [25]:

$$\Gamma_c = \frac{8k\left(T_0\right) k_B T_0^2}{U(H)\, \Delta E l^2} \tag{1.48}$$

where T_0 is the temperature of the sample boundary, $k\left(T_0\right)$ is the thermal conductivity at $T = T_0$, $U(H)$ is the energy barrier and l is the characteristic length of the sample. Magnetic deflagration can be initiated experimentally, either by heating one side of the sample [29–31], by surface acoustic waves [22] or by sweeping the magnetic field through the resonance [20, 32]

1.7.2.1 Thermally Driven Deflagration Front

A propagating deflagration front is a one-dimensional problem. The deflagration front propagates in one direction and has a flat and smooth profile. The stability of the flat front can be seen by assuming that a portion on the front gets ahead of the rest. Then

the heat from this portion starts to flow sideways. This will speed up the rest of the front left behind and also slow down the leading portion causing a flat front.

In the deflagration process there are two characteristic timescales. The first is the thermal diffusion timescale

$$\tau_d \simeq \frac{\delta^2}{\kappa}$$

where $\kappa = \frac{k}{C_{ph}}$ is the thermal diffusivity and δ is the width of the hot part of the front. The second is the burning timescale which is the chemical reaction timescale given by

$$\tau_b = \tau_0 \exp\left(\frac{\Delta E}{k_B T_f}\right)$$

where τ_0 is the attempt time, and T_f is the temperature of the front that also adverted as the flame temperature. The width of the front can be approximated by equalizing the two timescales $\tau_d \simeq \tau_b$ leading to $\delta = \sqrt{\kappa \tau_b}$. The front propagates at a characteristic speed v, which equals the width over the burning rate:

$$v \simeq \sqrt{\frac{\kappa}{\tau_b}} = \sqrt{\frac{\kappa}{\tau_0}} \exp\left(-\frac{U(H)}{2k_B T_f}\right) \tag{1.49}$$

where the flame temperature is given by:

$$T_f = \frac{\Theta_D}{\pi}\left[\frac{5 n_i \Delta E}{3 k_B \Theta_D}\right]^{1/4} \tag{1.50}$$

where Θ_D is the Debye temperature and n_i is the fraction of spins in the excited state [25].

In brief, the Chudnovsky-Garanin Theory of deflagration captures the main features found in the experiments. However, although some ignition experimental results agree with it in detail the theory does not provide a fully satisfactory description of the magnetic field gradient and sweep rate dependence of ignition and front velocity of the deflagration. As we shall see in measurements presented in section 4.3.

Chapter 2

Previous Work

2.1 The Magnetization of Fe_8

The magnetization of Fe_8 molecules as a function of an external field is presented in Figures 1.1 and 2.1, exhibiting hysteresis loops which have steps at well defined field values [5]. In Figure 1.1 one can see the temperature dependence of the "staircase" structure above 0.4 K at a constant sweep rate. Above 0.4 K there is thermally assisted tunneling and therefore wider steps in the magnetization. In Figure 2.1, five curves taken at 40 mK are shown, where the external field changed at five different sweeping

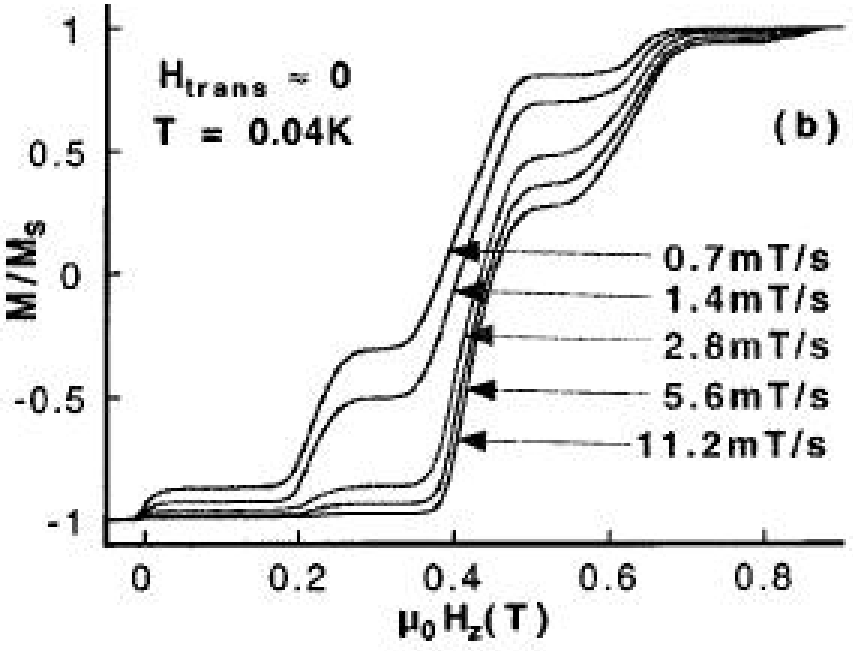

FIGURE 2.1: Field sweeping rate dependence of hysteresis loops[5]

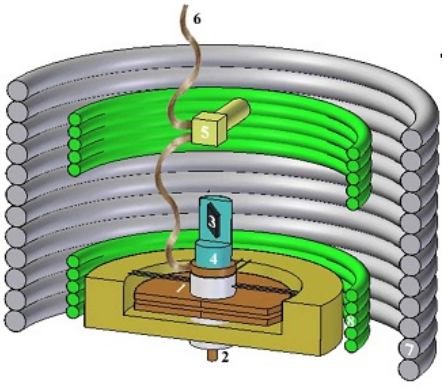

FIGURE 2.2: Cross sectional view of the Faraday balance with: (1) movable plate of the capacitor (2) screw for capacitor's fixed plate height adjustment (3) sample (4) a fluorocarbon-based polymer (5) gold-plated casing of the thermometer (6) thermal link to the DR mixing chamber (7) main coil (8) and gradient coils [1].

rates. The steps for all sweeping rates occur at the same field values, but the height of the step is different for the different rates. At a higher sweep rate a smaller fraction of molecules can relax by resonant quantum tunneling at lower critical fields. Therefore, more molecules are left in the excited state and the steps at higher critical fields are increased in height as the sweeping rate increases.

2.2 Radiation from Fe_8

Radiation emission from an Fe_8 single crystal was suggested by Shafir and Keren after the discovery of a jump in the temperature at each step in the magnetization curve [1]. The experimental setup is shown in Figure 2.2. The magnetization was measured using a Faraday force magnetometer, and the temperature was measured using a 2.2 $K\Omega$ RuO_2 thermistor in a gold coated casing. The results can be seen in Figure 2.3. Since the entire system is in a vacuum, the only ways that the energy could reach the thermometer is by radiation or via the copper thermal link. In another experiment the thermometer was moved to a separate thermal link to the mixing chamber, and the line of sight between the sample and the thermometer was blocked by covering the sample with a copper cylinder. The results are depicted in Figure 2.4. The steps in the magnetization were still seen, but the spikes in the temperature were not. The conclusion was that the thermometer heats up from bursts of photons from the sample. This Radiation could be in the form of Superradiance (see Sec 1.6).

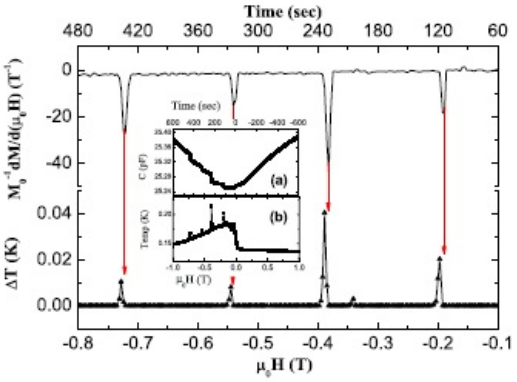

FIGURE 2.3: Normalized derivative of the magnetization and temperature spikes vs magnetic field. Raw data is in the inset: (a) magnetization and (b) temperature vs magnetic field. Steps in the magnetization indicate QTM in the sample.

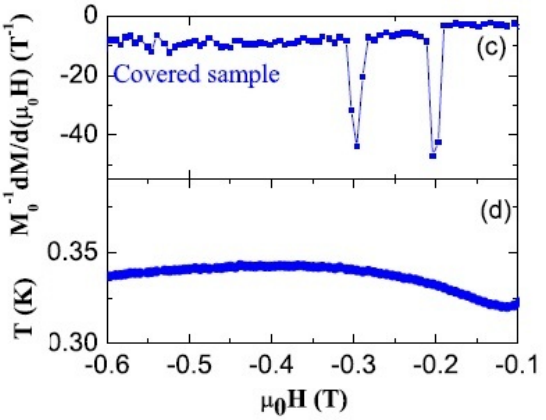

FIGURE 2.4: The normalized derivative of the magnetization (c) and temperature (d) vs magnetic field (same sweeping direction) with covered sample. The change in the magnetization is not followed this time by an increase in the temperature.

Bal et al.[33] showed in 2005 that a resonant microwave radiation applied to a single crystal of the molecular magnet Fe_8 induces changes in the sample's magnetization as shown in Figure 2.5. This indicates an interaction between the radiation and the spin. Transitions between excited states are found even though at the nominal system temperature these levels have a negligible population. They also find evidence that the sample heats significantly at resonance fields. In addition, the heating is observed after a short pulse of intense radiation has been turned off, indicating that the spin system is out of equilibrium with the lattice.

2.3 Measurements of Magnetic Deflagration

Crystals of Mn_{12}, which is an SMM similar to Fe_8, often exhibit an abrupt and complete reversal of the magnetization from one direction to the other in a process called "Magnetic Avalanches" as first reported by Paulsen and Park [19]. Suzuki et al. reported local time-resolved measurements of those avalanches in single crystals of Mn_{12}-acetate. They measured a narrow interface avalanche that had propagated through the crystal at a constant velocity of about 10 m/sec which is roughly two orders of magnitude smaller than the speed of sound. This process, illustrated schematically in Fig. 2.6, is closely analogous to chemical combustion: the propagation of a flame front through a flammable chemical substance, and referred to as chemical deflagration. Those avalanches occurred in a stochastic way, both at resonant matching fields, and away from them. [20].

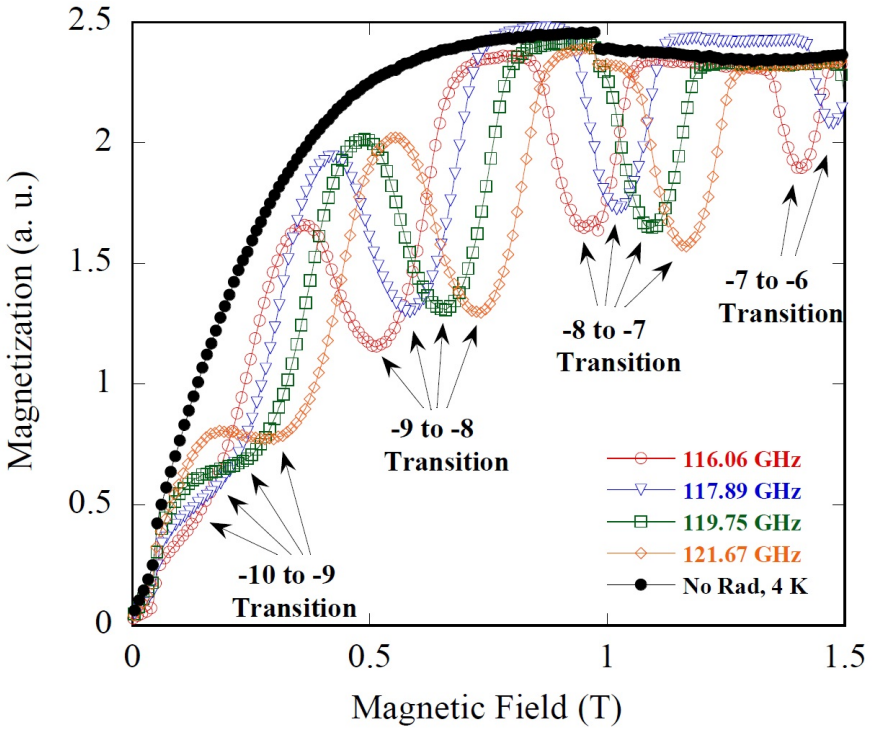

FIGURE 2.5: Equilibrium magnetization as a function of field, with and without the presence of radiation, as indicated. The dips in magnetization occur when the applied radiation frequency matches the transitions between states with the indicated magnetic quantum numbers. The applied radiation power and cavity Q were 1217 mW and 15002500, respectively, depending on the frequency. The abrupt jumps in the data, most conspicuous just below 1 T, are due to instrumental artifacts.[33]

Later, Hernandez *et al.* reported a controlled ignition of the deflagration in Mn_{12} by surface acoustic waves and saw that the speed of the deflagration exhibits maximum on the magnetic field at the tunneling resonances. They suggested a novel physical phenomenon: quantum assisted deflagration [22]. In 2010 Velez et al. found deflagration in the inter-metallic compound Gd_5Ge_4 with a good fit into the theoretical framework of deflagration [34].

Avalanches and superradiance are competing processes. For SR, no thermal transitions are assumed, and the SR pulse should be much faster than the energy release from the avalanche. In addition, after the avalanche occurs, all the molecules are at the ground state and no further steps in the magnetization can be seen.

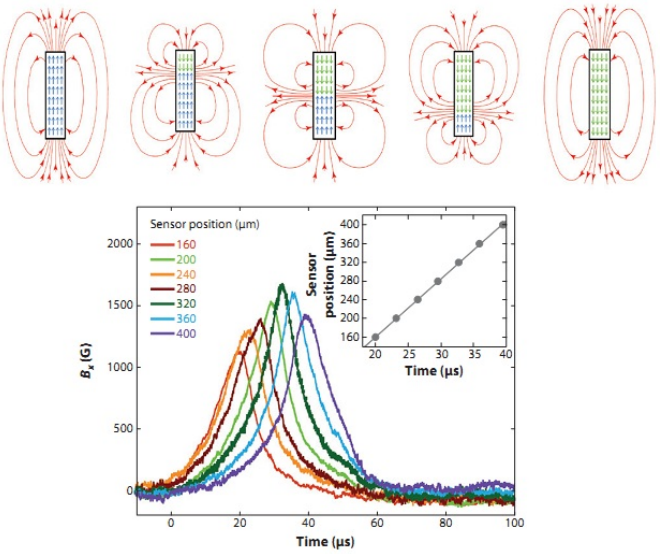

FIGURE 2.6: (Upper panel) Schematic diagram of magnetic field lines as spins reverse direction during a magnetic avalanche traveling from top to bottom of a Mn12-ac crystal. (Lower panel) The local magnetization measured as a function of time by an array of Hall sensors. Each peak corresponds to the bunching of the magnetic field lines as the deflagration front travels past a given Hall sensor [8].

Chapter 3

Experimental Methods

The preparation and orientation of the Fe_8 samples are described in section 3.1. In order to have pure, temperature-independent, quantum tunneling as mentioned in section 2.1 the experiment was performed inside a dilution refrigerator described in section 3.2.

The first objective of this research was to investigate the radiation emanating from the Fe_8 in the QTM process. In order to measure the wavelength of the radiation, a design with two filters was chosen, one with a band-pass filter around 100 Ghz and the other that blocked the 100 Ghz radiation. This design required two different optical paths from the sample to the detectors. Unlike the Shafir *et al.* experiment described in section 2.2, the magnetization needed to be measured in a way that would not block the line of sight. Therefore, Hall sensors were chosen for the magnetization detection. The design is described in section 3.3.

The Hall sensors are able to measure the local magnetic field in several locations under the sample in resolution that can be chosen in the manufacturing process. Therefore it can measure a spatially resolved magnetization.

The second objective of this research was to see how the magnetization changes as a function of location and to search for avalanches in the Fe_8. The discovery of avalanches in the Fe_8 and its analysis in the framework of magnetic deflagration as explained in section 1.7 led to the designing of an additional experiment to measure the thermal diffusivity of the Fe_8 as described in section 3.8.

3.1 Sample preparation and orientation

Single crystals of $[(C_6H_15N_3)_6Fe_8O_2(OH)_12]Br_7(H_2O)Br{\cdot}8H_2O$, abbreviated as Fe_8, were synthesized and oriented by the following steps:

3.1.1 Synthesis of $(C_6H_15N_3)FeCl_3$

4 ml of ethanol with 0.5 g 1,4,7-triazacyclononane (tacn) were added to a solution of $FeCl_3{\cdot}6H2O$ (3.5 g) in ethanol (100 ml). The resulting bright yellow precipitate of (tacn)FeCl3 was filtered off, washed with ethanol, and air-dried (∼0.25 g) [35].

3.1.2 Synthesis of Fe_8

0.25g of (tacn)FeCl3 was dissolved in 20 ml H_2O and 2 ml pyridine, while rotating the entire solution for about 15 min. Then 5 g of NaBr was then added to the solution. Contrary to Wieghardt *et al.* [9], nothing happened after 24 hours. After two-three weeks, brown crystals of Fe_8 separated out. The maximum size of the synthesized single crystals were about $3 \times 2 \times 1$ mm^3 as can be seen in Fig. 3.1 [9].

3.1.3 Orientation of the crystals

A schematic view of an Fe_8 single crystal and its crystallographic axes are shown in Figure 3.2. The unit cell parameters are: $a = 10.522\mathring{A}$ $b = 14.05\mathring{A}$ $c = 15.00\mathring{A}$ $\alpha = 89.90°$ $\beta = 109.65°$ $\gamma = 109.27°$ [9].
The faces of the crystal are well distinguished using a regular microscope and the sample was placed with the easy axis pointing to the $\hat{z}$ direction.

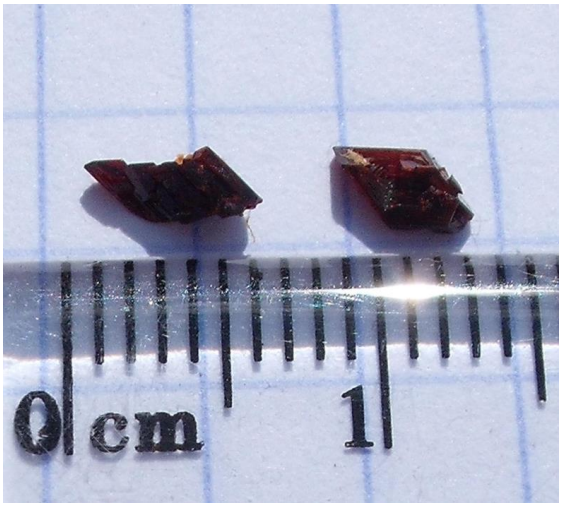

FIGURE 3.1: Fe_8 crystal grown in the Technion

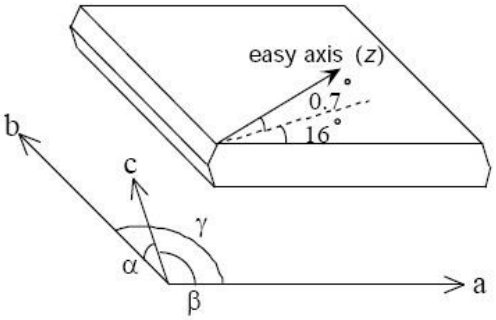

FIGURE 3.2: Crystal shape - schematic view of the anisotropy axes and the crystal axes

3.2 Dilution Refrigerator

The ^{3}He-^{4}He dilution refrigerator (DR) was used for all the magnetization measurements at the sub-Kelvin temperature range. The principle of operation of the DR was originally proposed by H. London in 1962 [36]. When a mixture of the two isotopes of helium is cooled below a critical temperature, it separates into two phases as shown in Figure 3.3. The higher (or lighter) "concentrated phase" is rich in ^{3}He and the heavier "dilute phase" is rich in ^{4}He.

The concentration of ^{3}He in each phase depends upon the temperature. Since the enthalpy (the sum of the internal heat in a system and the product of its volume and pressure) of the ^{3}He in the two phases is different, it is possible to cool the system by "evaporating" the ^{3}He from the concentrated phase into the dilute phase.

Although the properties of the liquids in the DR are described by quantum mechanics, it is possible to understand the cooling process in a classical way: let's regard the concentrated phase of the mixture as liquid ^{3}He, and the dilute phase as ^{3}He 'gas' which moves through the liquid ^{4}He without interaction. This 'gas' is formed in the mixing chamber at the phase boundary. This goes on even at the lowest temperatures because the equilibrium concentration of ^{3}He in the dilute phase is still finite, even as the temperature approaches absolute zero.

When the refrigerator is started the 1K pot is used to condense the ^{3}He/^{4}He mixture into the dilution unit. It is not intended to cool the mixture enough to set up the phase

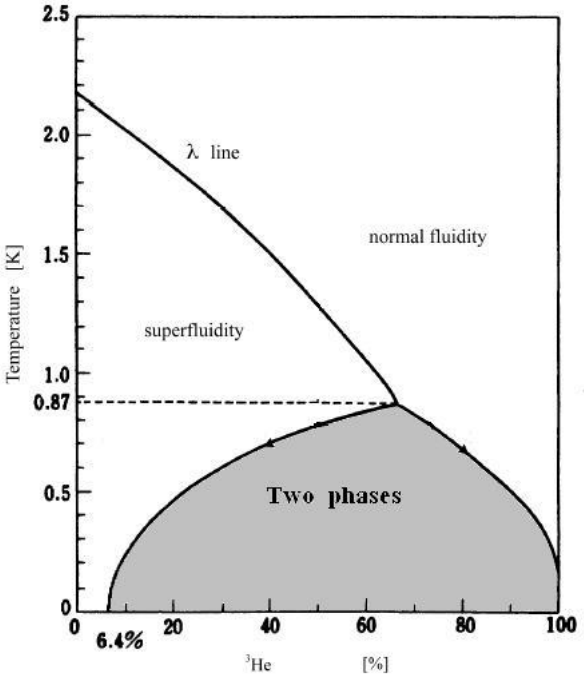

FIGURE 3.3: Phase diagram of $^3H/^4H$ [37]

boundary, but only to cool it to $\sim 1.5K$. The still is the first part to cool below 1.5 K. It cools the incoming ^{3}He before it enters the heat exchangers and the mixing chamber, and phase separation typically occurs after a few minutes (below 0.87 K).

If the ^{3}He concentration in the mixture is good, the phase boundary is inside the mixing chamber, and the liquid surface is in the still. ^{3}He is pumped away from the liquid surface in the still, which is typically maintained at a temperature of 0.6 to 0.7 K. At this temperature the vapor pressure of ^{3}He is about 1000 times higher than that of ^{4}He, so ^{3}He evaporates preferentially. A small amount of heat is supplied to the still to promote the required flow.

The concentration of ^{3}He in the dilute phase in the still therefore becomes lower than it is in the mixing chamber, and the osmotic pressure difference drives a flow of ^{3}He to the still. The ^{3}He leaving the mixing chamber is used to cool the returning flow of concentrated ^{3}He in a series of heat exchangers (sintered silver heat exchangers are used to decrease the thermal boundary resistance between the liquid and the solid walls). The room temperature vacuum pumping system is used to remove ^{3}He from the still, and compress it to a pressure of a few hundred millibars. The experimental apparatus is mounted on the mixing chamber, ensuring that it is in good thermal contact with the diluted phase.

3.3 Experimental Setup

The experiment was performed below 0.4K in a Dilution Refrigerator (DR) described in section 3.2. In figure 3.4 is shown the experimental setup which was located inside the inner vacuum chamber (IVC) of the DR. As implied from its name, the experiment was performed in a vacuum and the heat was conducted via the cold fingers to the mixing chamber of the DR. A detailed setup for the deflagration measurement is presented in Fig. 3.5

The sample with the Hall sensors, described in section 3.4, was located in the middle of a copper cylinder which was also thermally linked to the mixing chamber. At even distances from the sample, two sets of filters described in sections 3.5 and 3.6, were screwed into the cylinder, one set of 80Ghz high-pass with 170GHz low-pass filters and the second set of 200Ghz high-pass filters that could be replaced by a thick aluminum plate that was able to block all the radiation.

Two sets of RuO_2 bolometers were located behind the filters relative to the sample, (section 3.7). The purpose of the cylinder was to act as a waveguide and ensure that the photons arriving at the thermistors are passing through the filters. If the radiation has a sharp peak around 100Ghz, a spike in the temperature should have been seen only from the bolometers located behind the band-pass filter system. If there was a similar peak in both bolometers then either there is a broad band radiation or no radiation at all and the heat arrived at the bolometers only through the cold fingers. In this case the next experiment would be to block the high-pass side with an aluminum plate. Then if radiation is present only the bolometer behind the band pass would have a peak. If the bolometers still had a similar peak we can conclude that we do not see radiation above the sensitivity of our system.

3.4 Hall Effect Sensors

The Hall voltage is given by:

$$V_H = R_H I B_z \tag{3.1}$$

where R_H is defined as the Hall coefficient: $R_H = \frac{E_y}{j_x B} = \frac{1}{ned}$. Thus it can be used to measure the magnetic field.

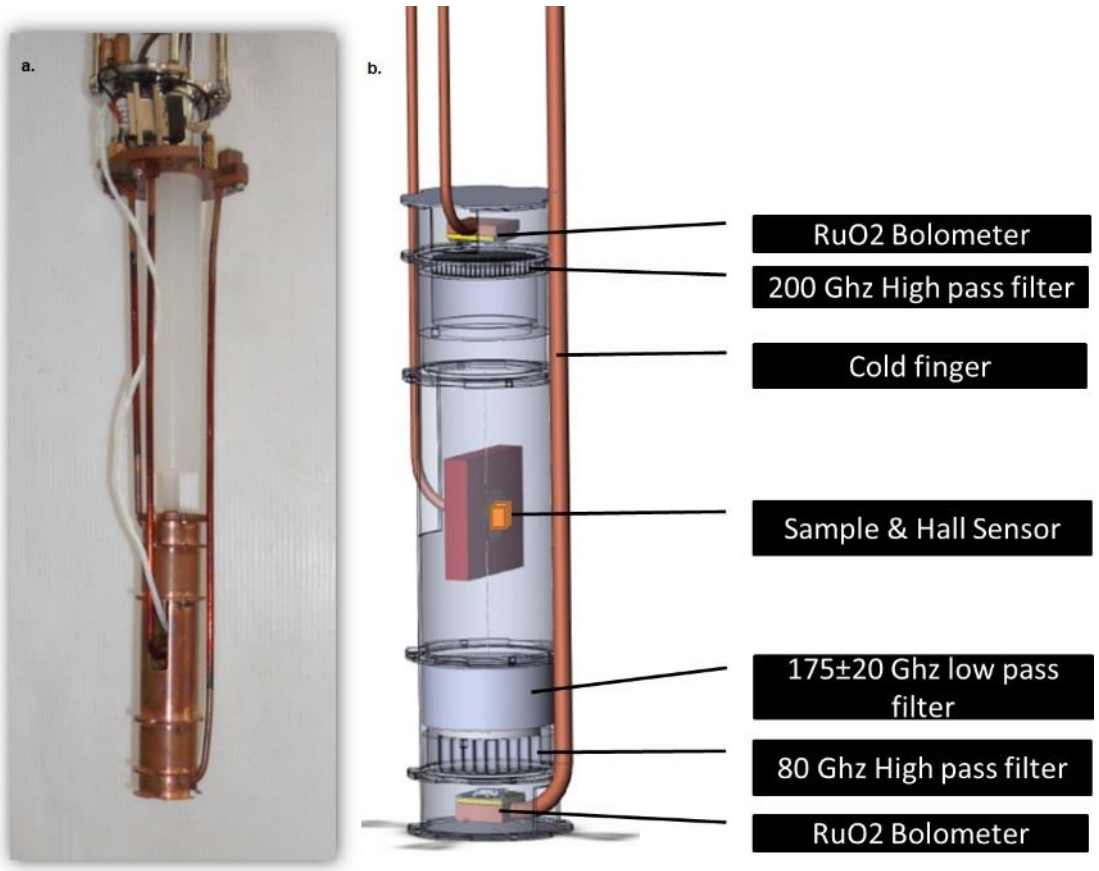

FIGURE 3.4: Experimental Setup: a. A live picture b. Technical drawing

A schematic view of Hall sensors array is shown in Figure 3.6. When a magnetic object is placed near the probe active areas, then the Hall voltage will be proportional to the sum of the external magnetic field B and the magnetic stray field which is linearly related to the magnetization.

We used an array of Hall sensors specially fabricated at The *Superconductivity Lab* from the *Weitzmann* institute using well established photolithographic and etching techniques with a typical active area of $100 \times 100\mu m$. The active layer in these sensors is a two-dimensional electron gas (2DEG) formed at the interface of GaAs/AlGaAs heterostructures. The size of the active area was chosen to be $100 \times 100\mu m$ in order to have 10 channels across the sample.

The array of Hall sensors was glued using GE varnish on a copper plate that sat in the center of a printed circuit board (PCB) from the front and the cold finger screwed from

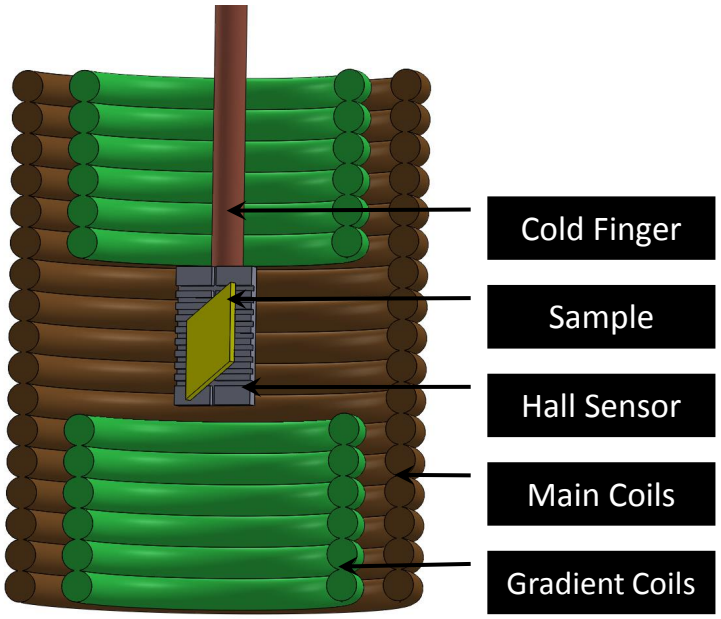

FIGURE 3.5: Detailed experimental Setup for deflagration measurement

the back. The Fe_8 sample was placed directly on the surface of the Hall sensor using Apizon-N grease. This was used with the dual function of holding the sample in place and protecting it from disintegration. A gold wire bonding was made between the Hall sensor array and the PCB. A picture of the front side is shown in Figure 3.7.

Ten twisted-pair wires were attached to the PCB, one pair for the excitation DC current of 10μA, and nine voltage channels to a differential amplifier specially made for the experiment with ten channels at $\times$500 amplification. The channels were distributed between seven 30 Hz low-pass filters, two channels with 200 Hz high-pass filters and one channel without any filtering. The measurements of hysteresis loops were performed using the low-pass channels in order to filter out the 50 Hz noise. The other channels were for measuring magnetic deflagration at high frequencies at a rate of 20 KHz.

3.5 Mesh Grid Low-Pass Filters

Metal mesh filters have been used in far infra-red and sub-millimeter wave instruments since the first publication by Ulrich [38]. Ulrich showed that the optical transmission properties of a metallic mesh can be modeled by considering the mesh to be a simple circuit element on a free space transmission line. He focused on the properties of two

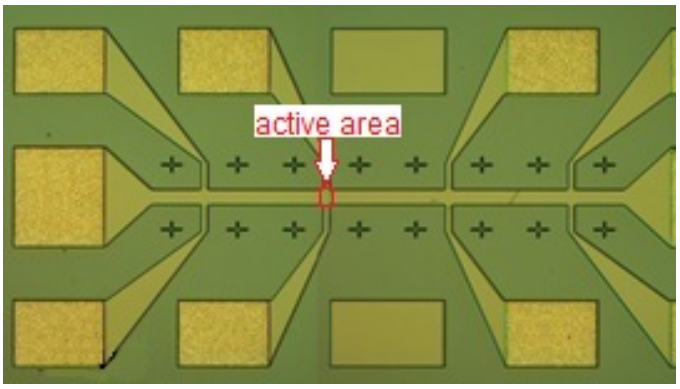

FIGURE 3.6: A schematic view of a Hall sensors array

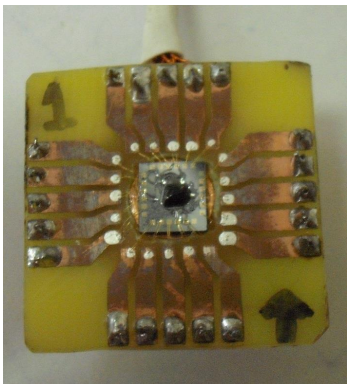

FIGURE 3.7: A picture of the front side of the magnetization detecting probe with the Fe_8 sample in the center.

types of mesh structure: a metallic grid with square openings; and a grid of metallic squares supported on a thin dielectric substrate.

Using the transmission line method, he modeled the behavior of each of these meshes as either a lumped inductance (square openings) or a lumped capacitance (free-standing squares). These two types of meshes are commonly referred to as inductive or capacitive meshes, and are shown in Figure 3.8.

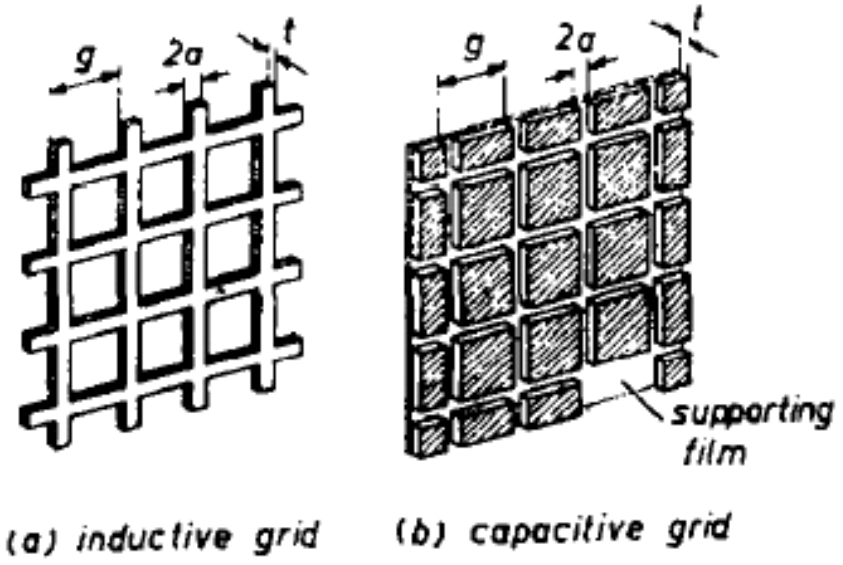

FIGURE 3.8: The inductive and the capacitive two dimensional grid [38]

Although the transmission can be calculated numerically, it is possible to understand the concept of mesh filters in more intuitive way [39]. If we combine the inductive and the capacitive grids such that they are complementary to each other, we have a conductive surface and therefore the sum of the reflected wave from both structures must equal the original incident wave.

So, the reflectance $R(\omega)$ relation is (assuming a perfect conductor):

$$R(\omega)_{inductive} + R(\omega)_{capacitive} = 1 \tag{3.2}$$

In an inductive grid the metal is continuous, and the electrons can move the "long" distances, thus matching the long wavelengths of the photons. So, at low frequencies, it will reflect all the incident waves, thus acting as a high-pass filter. From Eq 3.2 we know that the grids are complementary to each other: therefore, a capacitive mesh will act as a low-pass filter.

The filters for this experiment were brought from Prof. Shaul Hanany's astrophysics group at the University of Minnesota, where they were previously used for measuring the Cosmic Background Radiation, which is also around 100 Ghz. Achieving a low-pass at 180 Ghz requires two filters, one with a cut-off at 180 Ghz that has a small transmission peak around 400 Ghz, and another filter with a cut-off around 288 Ghz to abolish the unwanted transmission peak. The transmission of the filters are plotted in Figure 3.9.

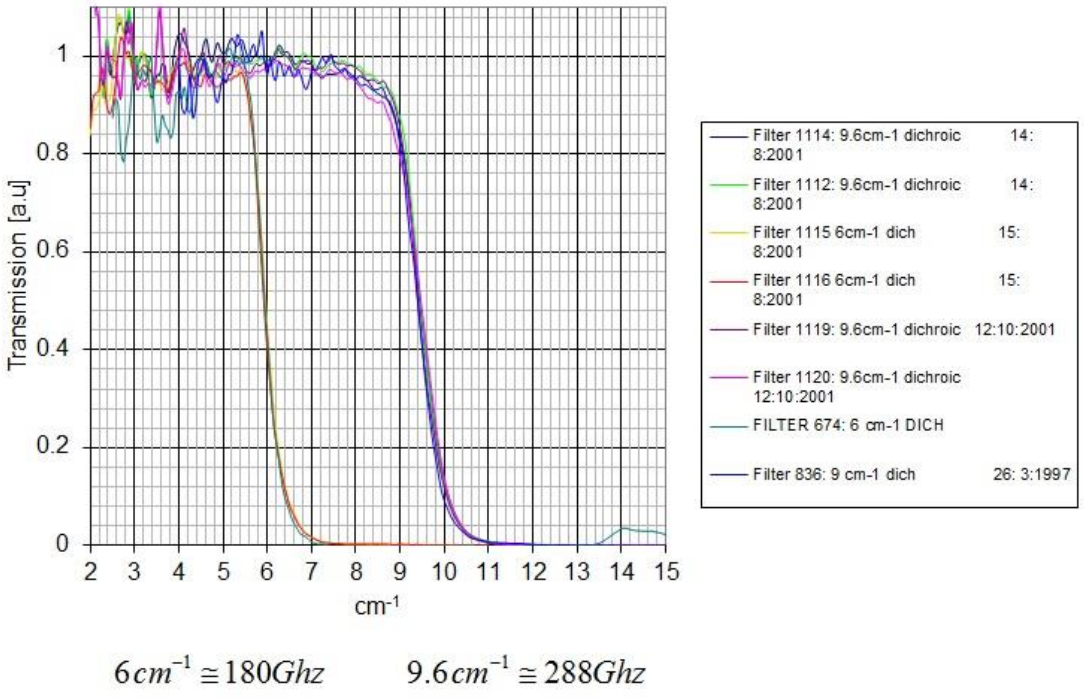

FIGURE 3.9: Transmission plots of the low-pass filters

3.6 Thick Grill High-Pass Filters

The thick grill inductive filter was developed to block the region of low frequencies where the capacitive grid is transparent. It consists of a thick metal plate with a hexagonal close-packed array of circular holes. A thin inductive mesh would serve the same purpose, but it does not have as sharp a cutoff and it is more expensive. The thick grill filter does not transmit frequencies below the lowest frequency propagating circular waveguide modes in the holes. The relation between the cut-off frequency and the hole diameter is an experimentally measured number:

$$\lambda_C = 1.706 \cdot d$$

where λ_C is the cut-off wavelength and d is the hole diameter [40].

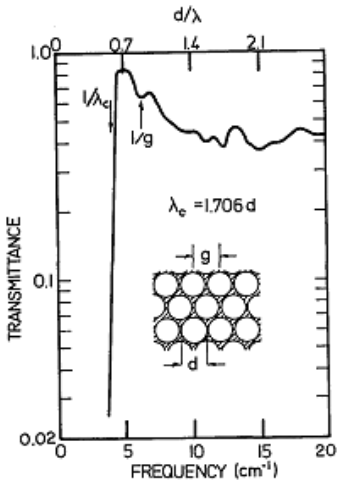

FIGURE 3.10: Transmission curve of a typical thick grill filter[40]

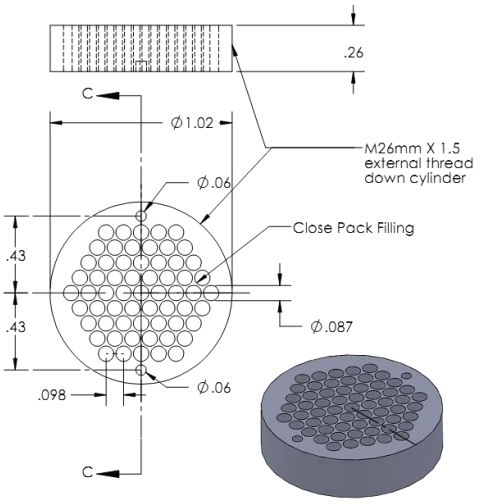

FIGURE 3.11: Technical drawing of the 80Ghz filter

The attenuation A in dB in the waveguide is proportional to:

$$A = \frac{l}{d} \cdot 30dB$$

where l is the thickness of the plate. A typical choice for an attenuation of about 90 dB is $l = 3d$. The transmission curve of a typical thick grill filter is shown in Figure 3.10, and the technical drawing of the 80 Ghz filter is shown in figure 3.11.

3.7 Ruthenium Oxide Bolometers

After passing the filters the radiation is to be detected using a RuO_2 thermistor mounted to a PCB in a configuration shown in Figure 3.12. The idea of this design is to have a weak and adaptable thermal link to the mixing chamber to control the relaxation time of the resistor after being heated by the radiation pulse. It is therefore convenient to use the PCB substrate layer of Glass Epoxy FR-4 as a thermal isolator placed between the cold finger and the absorbing area.

The absorbing area consists of two copper sheets $11mm \times 4mm \times 35\mu m$ in size, with a gap between them for the RuO_2 thermistor as shown in Figure 3.12. The thermistor is a standard Lake-Shore RX-202A with a typical temperature-depended resistance and is shown in Figure 3.13. The thermistor is welded from both sides to the copper sheets and GE-varnish coated copper wires are welded to the sheets for the resistance measurement. The wires are thermally linked to the mixing chamber through the measurement connector. The resistance is measured using a voltage divider and a lock-in amplifier in

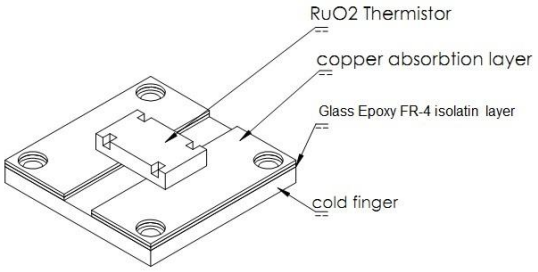

FIGURE 3.12: Technical drawing temperature sensing device

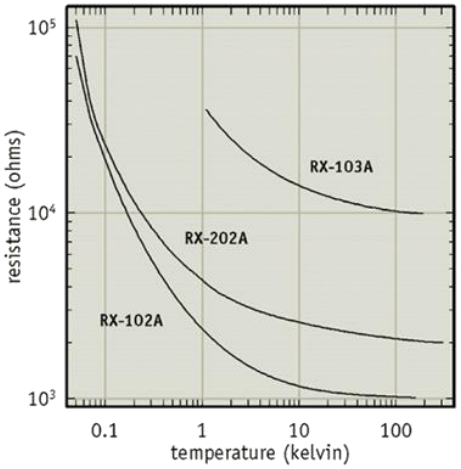

FIGURE 3.13: Typical resistance values of RuO2 thermistors. We are using the RX202A

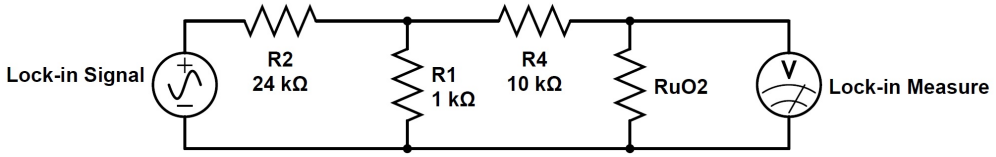

FIGURE 3.14: Circuit diagram for Bolometer resistance measurement

order to have a low excitation current of 10 nA. The voltage divider is shown in Figure 3.14.

3.8 Thermal Diffusivity

The thermal diffusivity measurements were carried out inside a HelioxVT He_3 Oxford Instruments refrigerator. The experiment was performed using two thermometers mounted on opposite sides of the sample and a heater on the hot side of the sample, whose configuration is shown in Figure. 3.15. The hot side is attached to the cold finger and is hot only after the heat pulse. The thermometers are RuO_2 films. The heater is a 2.2 KΩ resistor. The hot side thermometer was placed between the heater and the sample. The cold side thermometer is between the sample and a teflon plate. It has a weak thermal link to the cold plate via the measurement wires only.

Additional RuO_2 film was placed on a symmetrical location on the cold side to act as a test experiment. This thermometer had an identical thermal link to the cold plate

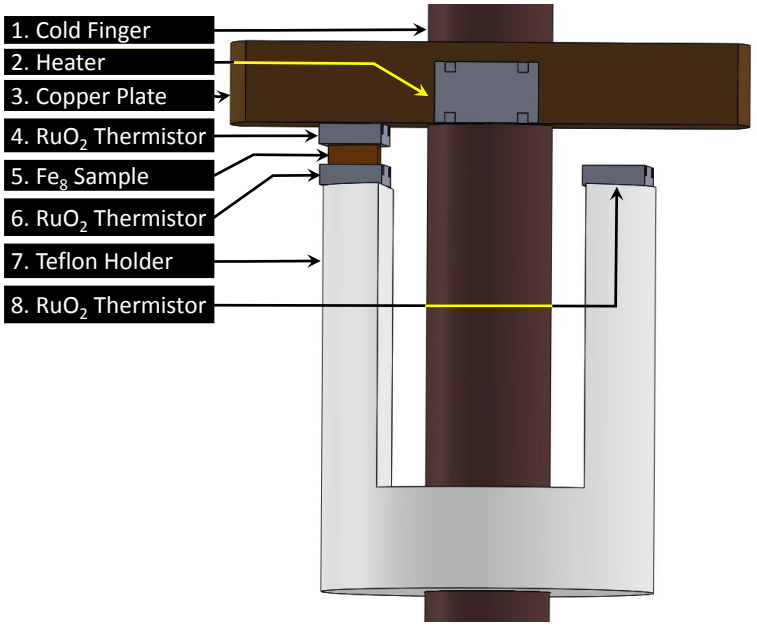

FIGURE 3.15: Thermal diffusivity experimental setup. Heat pulse is provided by heater 2. Thermistor 4 measures T_{hs} and Thermistor 6 measures T_{cs}. Thermistor 8 is used to determine heat leaks via the measurement wires.

of the He_3 refrigerator through the wires, and is placed in a symmetrical location on the teflon holder under the hot copper plate. The only difference between the cold side thermometer and the test thermometer is that the test thermometer is not in contact with the sample and the hot side is.

The purpose of the test thermometer is to ensure that the heat pulse reaching the cold side arrives from the sample only and not through the measurement wires of the holder. We tested several heat pulses and chose one that fits this condition. The heat pulse is generated by applying 8 V to a 2.2 KΩ resistor for 1 msec using a function generator, which also acts as the trigger for starting the RuO_2 voltage measurement. The system has also been tested by repeating the measurement without the sample to ensure again that the recorded heat on the cold side flows through the sample and not through the wires.

Chapter 4

Results And Discussion

In the experiment the molecules were polarized by applying a magnetic field of ± 1 T in the easy axis direction $\hat{\mathbf{z}}$. Afterwards, the magnetic field was swept to ∓ 1 T. The sweep was done at different sweep rates. During the sweep we recorded the Hall voltages, the external field, and the bolometers' voltage. From the raw field-dependent voltage of each sensor, a straight line was subtracted. This line is due to the response of the Hall sensor to the external field. The line parameters are determined from very high and very low fields where no features in the raw data were observed. Then the voltage was normalized by the voltage at a field of 1 T where the molecules are fully polarized. Thus, the normalized voltage provided M/M_0, where M is the magnetization and M_0 is the saturation magnetization.

In our experiments, we found that Fe_8 samples can be divided into two categories: those that do not show avalanches, which have multiple magnetization steps regardless of the sweep rate, and those that show avalanches where the number of magnetization steps depends on the sweep rate. In Fig. 4.1, we present the normalized signal as detected by one of the Hall sensors from samples of both categories. The bottom abscissa is for a sweep where the field decreases from 1 T. The top abscissa is for a sweep where the field increases from -1 T.

For a sample of the first category, the magnetization shows typical steps at intervals of 0.225 T. No step is observed near zero field. In addition, the hysteresis loop's coercivity increases as the sweep rate increases. These results are in agreement with previous measurements on Fe_8 [5]. They are presented here to demonstrate that the Hall sensors are working properly, that their signals indeed represent the Fe_8 magnetization, and that in some samples all magnetization steps are observed.

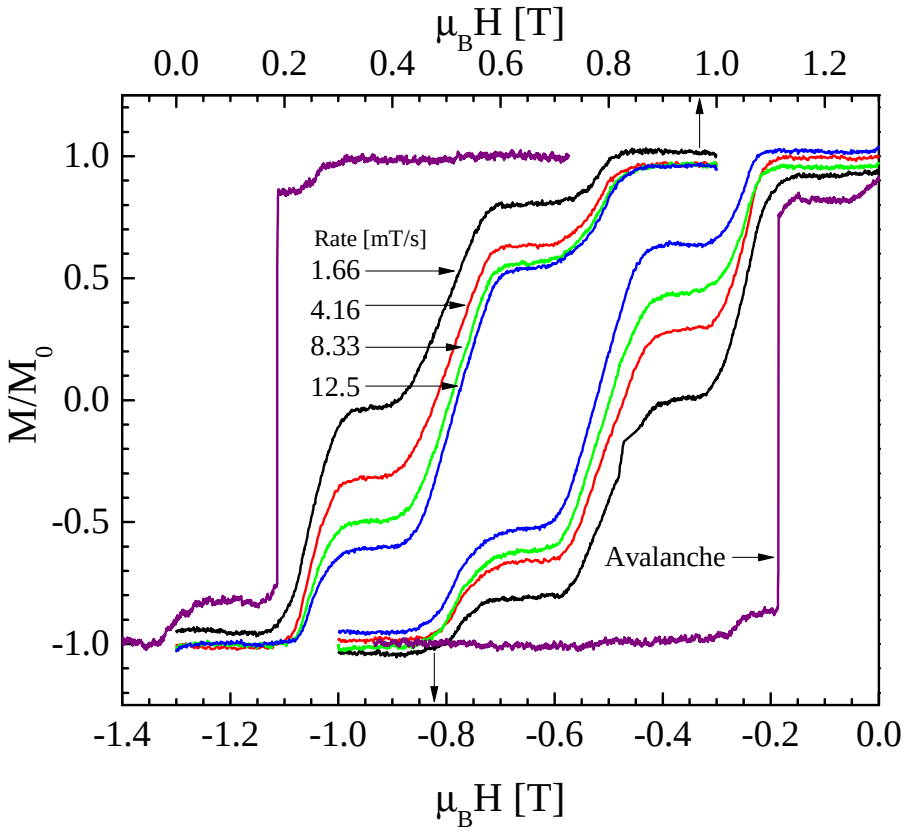

FIGURE 4.1: Fe_8 hysteresis loops with multi-step magnetization jumps, at different sweep rates, and a hysteresis loop with an avalanche. The fields for the positive sweep rates are given by the bottom abscissa, and for the negative sweep rates by the top abscissa.

For a sample of the second category, there is a small magnetization jump at zero applied field, followed by a nearly full magnetization reversal at a field of 0.2 T in the form of deflagration. This kind of spontaneous, full magnetization reversal in the form of deflagration is found in various kinds of magnets [34, 41]. However, in all Fe_8 samples tested, deflagration occurred only at the first matching field. We could not tell in advance whether a sample was of the first or second category. We always worked with samples of approximately the same dimensions ($3 \times 2 \times 1$ mm^3). This is in contrast to Mn_{12}, where deflagration is associated with large samples [25].

4.1 4.2 Kelvin measurement

A measurement of the magnetization was performed at 4.2 K to ensure that the steps in the magnetization derive from the QTM process. The results at 4.2 K and 0.2 K are

presented in Figure 4.2. Indeed a paramagnetic behavior is detected at 4.2 K and no sweep rate dependence is seen.

4.2 Radiation measurements

We tested for electromagnetic radiation in samples from both the categories mentioned previously, each weighing roughly 20 mg. In the avalanche process, a large amount of heat was released and a clear tunneling front was present [32]. Without the avalanche, the temperature of the sample is expected to remain low compared to the energy barrier. In this case, a unique quanta of energy should be emitted in the tunneling process.

We tested the response of the bolometers to a pulse of radiation in-situ by replacing the Fe_8 sample with two Fairchild LED56 diodes that were pointing in both directions of the cylinder. The diodes were thermally connected directly to the 1 K pot of the DR for better cooling power and for minimizing their heating affect on the bolometers. The diodes' bias power was selected so as to give a similar energy pulse to the bolometers as a tunneling event with the Fe_8 sample (see below). In Fig. 4.3 we plot the open and blocked bolometers voltage as a function of time after energizing the diodes. The solid line indicates the voltage across the diodes as a function of time.

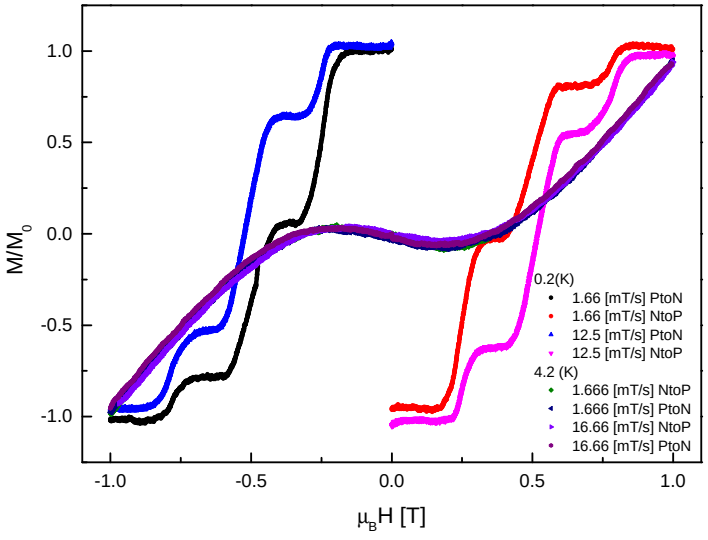

]

FIGURE 4.2: Amplified Hall Voltage, proportional to the magnetization, as a function of the magnetic field. At two temperatures and two sweep rates.

The bolometer's voltage was proportional to the temperature of the thermistor and therefore to the power deposited. The temperature of the bolometer which was open to radiation increased as soon as the diodes' power was turned on. Two seconds later, the thermal energy from the diodes and the copper cylinder reached both bolometers simultaneously. The instantaneous increase of the open bolometer voltage is the most significant indication of radiation. This increase was detected with a signal-to-noise ratio (SNR) of 100 in amplitude (see the blue trace in Fig. 4.3) and an even larger SNR in time by the temporal separation between the early and late pulses.

We also tested the ability of the two bolometers to detect thermal energy. The inset of Fig. 4.3 shows the case where the sample area was heated by a resistor. The power and duration of this heat pulse were again similar to that produced by the Fe_8 sample (see below). In this case the temperature of both bolometers increased simultaneously to the same temperature. Therefore, by subtracting the voltage of the bolometers, and focusing on the time before thermal energy arrived at the bolometers, we obtained the signal of electromagnetic radiation only. This signal is also depicted in Fig. 4.3 by a blue curve. It decays slowly since the cooling power of the two bolometers is different due to different distances from the mixing chamber. The early time signal, up to ~ 4 sec, demonstrates that we can clearly detect electromagnetic radiation emitted from the diodes using our experimental setup.

The results of our experiment in the case of an avalanche are shown in Fig. 4.4. The sweep rate is 1.67 mT/sec. The left ordinate is the bolometers' voltage. The right ordinate is the normalized magnetization M/M_0. The bottom abscissa shows the field values and the top abscissa shows the time. When the external field is at matching value a QTM occurs followed by a rise in the bolometers' voltage indicating a rise in the temperature. However, there is no observable difference in the rise time or voltage amplitude between the opened and the blocked bolometer. The bolometers' voltage started to rise 2 sec after the avalanche. This is a time interval similar to the diode experiment, and is due to thermal energy arriving at the bolometers. We therefore conclude that no significant photon contribution in the band between 70 and 180 GHz is detected when an avalanche is taking place.

To place an upper limit on photon emission during the avalanche process, we copied the photon signal from the first 4 seconds of the diode experiment (the blue curve in Fig. 4.3), scaled it to a range of fractions between 1% and 20% of the thermal energy signal recorded by the closed bolometer, and added it to the open bolometer signal. The goal was to assess the photon signal level that, if it was present, would clearly be

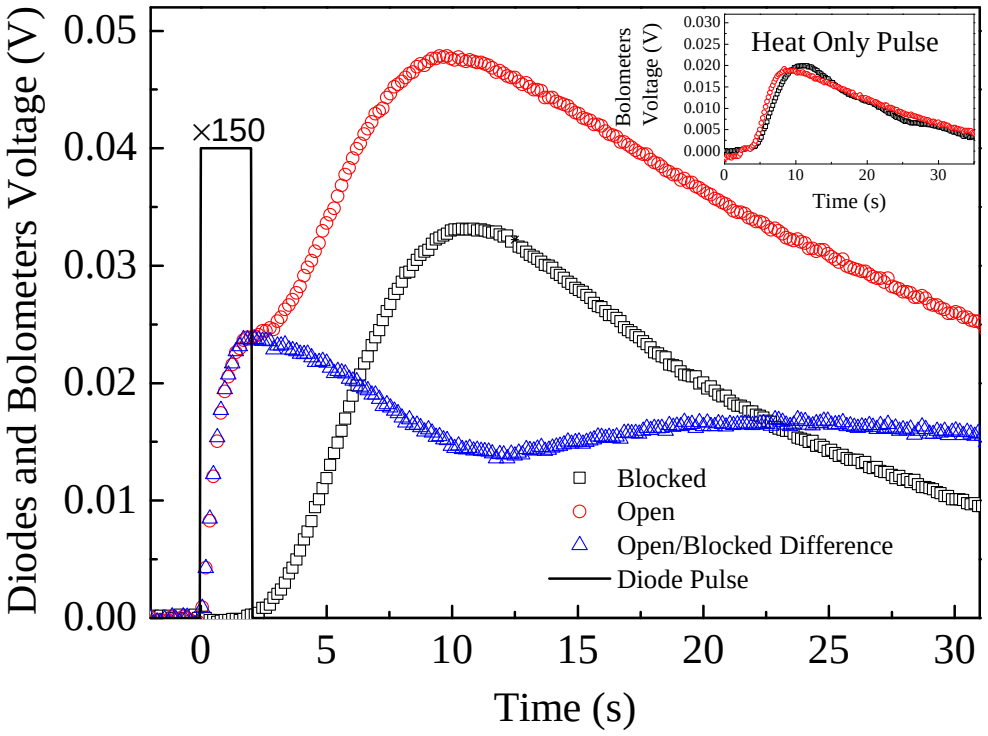

FIGURE 4.3: The response of the bolometers to a test radiation and thermal energy pulses. The solid line is the voltage pulse applied to the light emitting diodes. The red and green symbols show the voltage developed across the open and blocked bolometers as their temperature increases due to the radiative pulse from the diodes. The blue symbols are the voltage difference. The difference within the first second represents the detection of a photon signal. The inset shows the same experiment but with an input of thermal energy into the sample using a biased resistor.

temporally separate from, and of higher amplitude relative to the signal of the closed bolometer. The case when the photon signal is scaled to 10% is shown in the Fig. 4.5. This is a case in which the open bolometer voltage clearly precedes the closed one temporally and levels off at a higher amplitude. By varying the fraction between 1% and 20% and considering the noise, we found that we could place an upper limit of 5%. That is, no more than 5% of the energy emitted by the molecular magnet had been converted to light. If it did, we would have detected it.

The experimental results when avalanche was absent are shown in Fig. 4.6. Here again we show the bolometers' voltage, magnetization, field, and time as in Fig. 4.4. The sweep rate is 0.34 mT/sec. Two clear transitions are observed in this experiment. Here the bolometers' voltage rose over a longer time, reducing the rise time resolution. Therefore, detecting photons without an avalanche is harder and can rely only on pulse amplitudes.

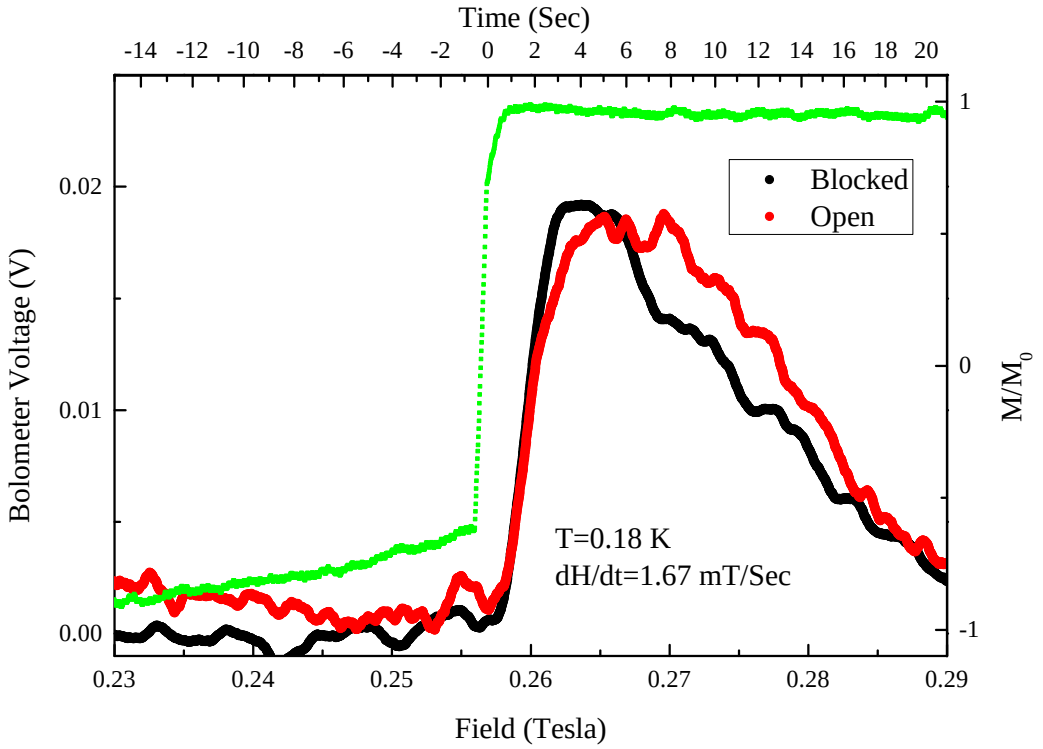

FIGURE 4.4: Magnetization and energy emission measurements done simultaneously on an Fe_8 molecular magnet after an avalanche. The left ordinate is the open and closed bolometers voltage, which is proportional to their temperature. The right ordinate is the normalized magnetization. No difference between the two bolometers is detected within the experimental sensitivity.

No amplitude difference was observed between the open and closed bolometers for either of the magnetic transitions.

Thus, we did not observe electromagnetic radiation emanating from the Fe_8 regardless of the sweep rate or the transition index n. If the molecules do emit radiation, it consists of less than 5% of the total energy release. A similar conclusion was drawn by Bal *et al.* regarding the Mn_{12} molecular magnet [42].

However, it is interesting to note that at the second transition it took the bolometers more time (a longer field interval) to cool down than at the first transition. There could be two possible explanations: (I) The lifetime of the $n = 2$ excited state is longer than the $n = 1$ state. This possibility stands in contrast to the lifetime measurements by Bahr *et al.* [43], although they were done at higher temperatures. (II) As we sweep the field there are more transitions from the metastable state to $n = 3, 4 \ldots$ excited states. As n increased the magnetization change becomes smaller but the energy released becomes larger. It is conceivable that we were unable to detect magnetically the higher

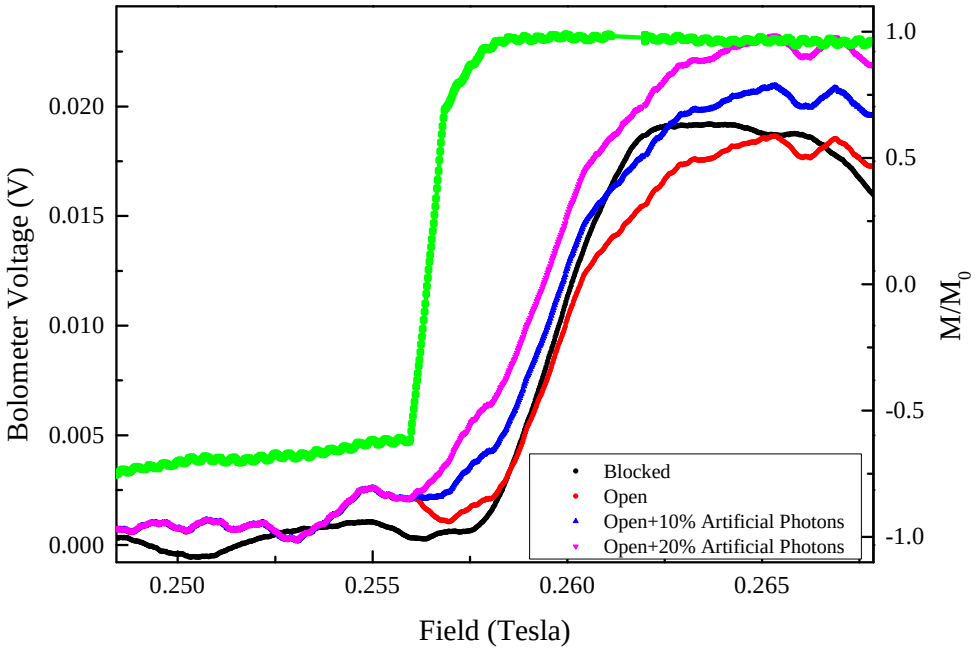

FIGURE 4.5: The experimental sensitivity of photon detection. Photons signal was copied from the first 4 seconds of the open bolometer in Fig. 2, normalized to 10% of the closed bolometer, and added to the open bolometer. A clear difference between open and closed bolometers can be seen. We thus set the experimental sensitivity of photons to 5% of the thermal (phonon) energy.

transitions but could detect their energy release. More experiments are required to distinguish between the two possibilities.

To summarize the radiation measurements section, we re-examine the possibility that Fe_8 emits electromagnetic radiation after a tunneling events using a specially designed experimental setup. Our results do not reproduce those reported earlier by Shafir and Keren [1]. We placed an upper limit of 5% on the amount of energy released by radiation, and conjecture that energy is released after tunneling in Fe_8 only in the form of thermal energy. This is important for understanding the role of phonons in the tunneling process.

4.3 Magnetic Deflagration Measurements

Our deflagration velocity measurements are based on local and time-resolved magnetization detection using a Hall sensor array as described in section 3.4. We found that it is possible to ignite the deflagration in the quantum regime ($T < 400$ mK) by sweeping

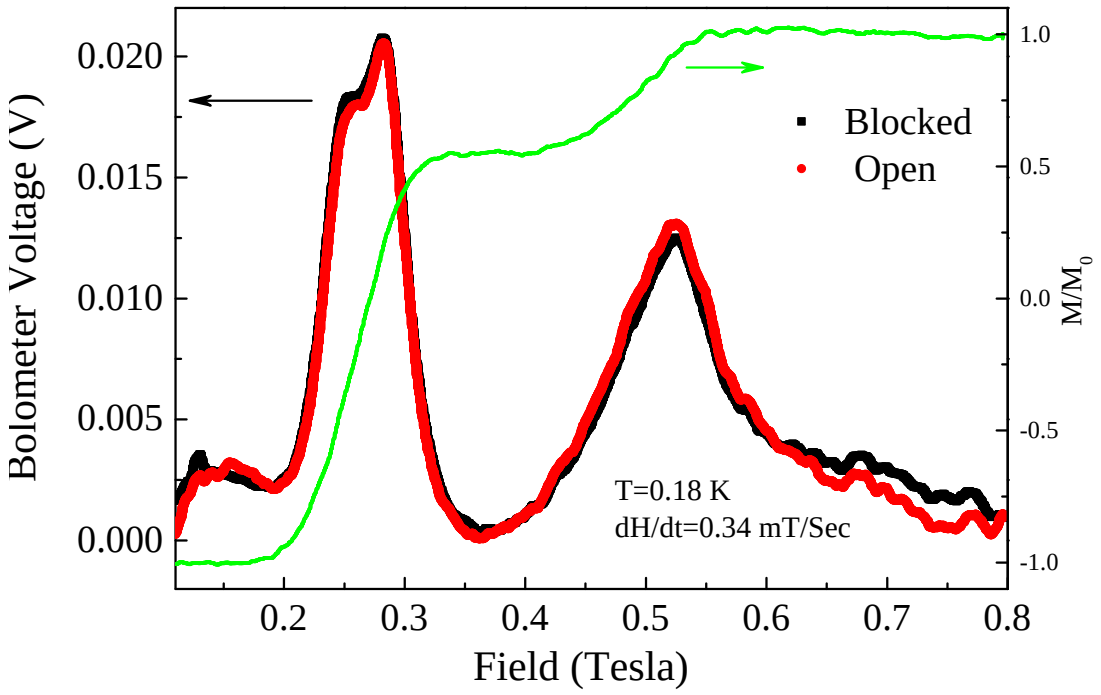

FIGURE 4.6: Magnetization and energy emission measurements done simultaneously on an avalanche free Fe_8 molecular magnet. The left ordinate is the open and closed bolometers' voltage, which is proportional to their temperature. The right ordinate is the normalized magnetization. No difference between the two bolometers is detected within the experimental sensitivity. The second bolometer voltage peak decays more slowly than the first one, with no noticeable magnetization changes at fields approaching 1 T.

the external magnetic field through a matching field, without external assistance such as phonons. In addition, we measured the deflagration velocity V_d for various sweep rates and applied field gradients.

Before measuring the deflagration velocity, note that the measurements in Fe_8 should be done with extra care. In deflagration there is a propagating front where spins reverse their direction. But since our Fe_8 measurements were done by sweeping the magnetic field through resonance, there is a similar front even without deflagration. This is demonstrated in the inset of Fig. 4.7. In this inset, a sample placed off the symmetry point of a symmetric field profile is shown. Thus, the sample experiences a field gradient. Due to this gradient, tunneling of molecules will start first at a particular point in the sample where the local field is at matching value. The spin reversal front will then propagate from that point to the rest of the sample as the external field is swept. In this case, pausing the field sweep will stop the magnetization evolution.

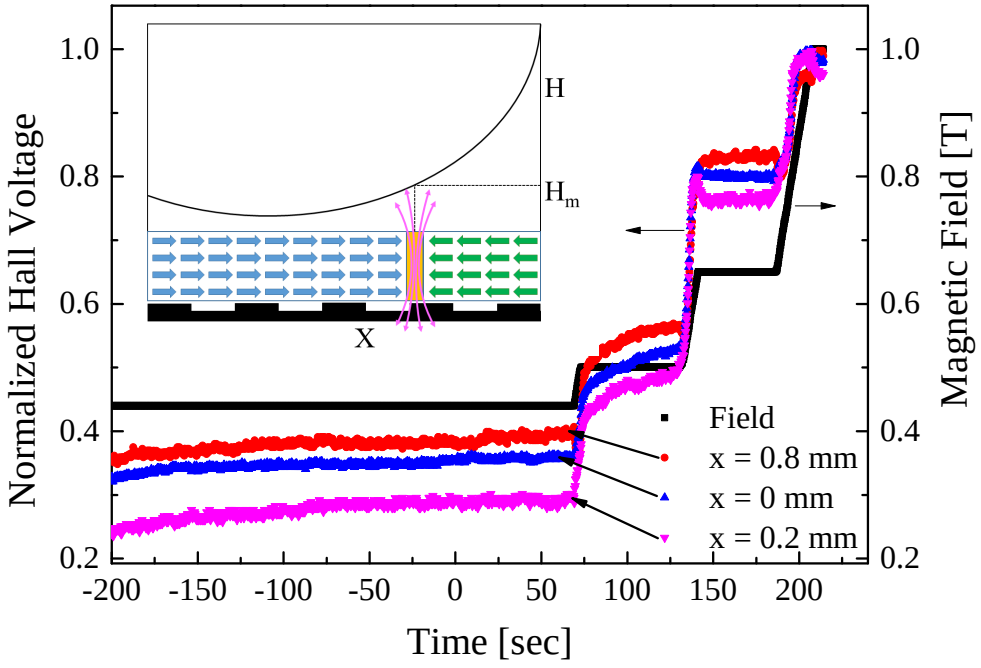

FIGURE 4.7: Magnetization as a function of time for a sample of the first type with no avalanche. The magnetization is measured via three different Hall sensors. The field is swept discontinuously. The solid (black) line shows the field value as a function of time on the right y-axis. The magnetization, presented on the left y-axis, changes only when the field changes. The inset demonstrates a tunneling front evolution in a case where the matching field H_m moves across the sample during a sweep. H is an instantaneous field intensity. It changes with time and varies in space. The tunneling region with mixed up and down spins has zero magnetization. The expelled magnetic induction $\mathbf{B}$ is detected by the Hall sensors.

This is demonstrated in Fig. 4.7 for a deflagration-free sample. The left ordinate is the normalized Hall voltage (solid symbols) from three different sensors on the array located at $x = 0, 0.2$ and 0.8 mm under the sample, where $\hat{x}$ is the easy axis direction. Each symbol represents a different sensor. The right ordinate is the applied magnetic field (line). The voltage and field are plotted as a function of time. We focus on fields before, near, and after the third transition in Fig. 4.1. For the most part, the magnetization changes only when the field changes, even in the middle of a magnetization jump. This means that the sample is subjected to some field gradients and a tunneling front propagates through the sample even without deflagration. It is possible to estimate the matching field front velocity as $V_m \sim 1.5 \times 10^{-4}$ m/sec from a typical transition width (0.1 T), a typical sweep rate (5 mT/sec) and the sample length (3 mm).

After calculating V_m we can proceed to estimation of the deflagration front velocity

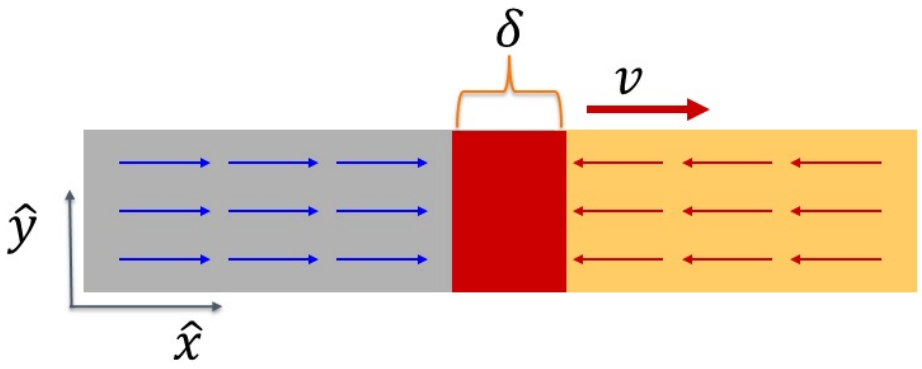

FIGURE 4.8: Illustration of an SMM sample undergoing a magnetic deflagration. The sample lies in the XY plane with the magnetization pointing in opposite directions from different sides of the sample, and zero magnetization front with a width of δ propagating in a velocity v.

V_d. The magnetic induction **B** from the sample is forced to point outward and toward the sensors, in order to maintain zero divergence [8]. The field configuration is also demonstrated in the inset of Fig. 4.7. This type of behavior is a clear indication of a magnetization reversal front propagating from one side of the sample to the other and can be calculated explicitly by taking the magnetic dipole:

$$\vec{B} = \frac{\mu_0}{4\pi}\left(\frac{2\vec{r}\,(\vec{\mu}\cdot\vec{r})}{r^5} - \frac{\vec{\mu}}{r}\right). \tag{4.1}$$

Since our Hall sensor measures the perpendicular field we look only at the $\hat{z}$ component:

$$B_z = \frac{\mu_0}{4\pi}\left(\frac{3z\,(\vec{\mu}\cdot\vec{r})}{r^5} - \frac{\mu_z}{r^3}\right). \tag{4.2}$$

When a sample undergoes an avalanche it can be represented as two cuboids with magnetization pointing in opposite directions separated by a zero magnetization area as presented in Fig. 4.8. For a start, we will calculate the field of a single cuboid which lies at the XY plane with the magnetization pointing in $\hat{x}$ direction, and with a dipole moment given by:

$$\vec{\mu} = m dx dy dz \hat{x}. \tag{4.3}$$

where m is the magnetic dipole density and the sample boundaries are:

$$\begin{aligned} x_1 < x < x_2 \\ -w < y < w \\ d_1 < z < d_2 \end{aligned} \tag{4.4}$$

Integrating over the dipole density gives the magnetic field in the $\hat{z}$ direction of a single cuboid:

$$\begin{aligned} B_z(x_1, x_2) &= \tfrac{3\mu_0 m}{4\pi} \int_{x_1}^{x_2} dx \int_{-w}^{w} dy \int_{d1}^{d2} dz \tfrac{xz}{(x^2+y^2+z^2)^{\frac{5}{2}}} = \\ &= \tfrac{3m\mu_0}{4\pi} \int_{x_1}^{x_2} dx \int_{d1}^{d2} dz \left(\tfrac{2xzb\left(3x^2+3z^2+2w^2\right)}{3(x^2+z^2)^2(w^2+x^2+z^2)^{\frac{3}{2}}} \right) = \\ &= \tfrac{3m\mu_0}{4\pi} \int_{x_1}^{x_2} dx \left(\tfrac{2wx}{3\left(x^2+d_1^2\right)\sqrt{w^2+x^2+d_1^2}} - \tfrac{2wx}{3\left(x^2+d_2^2\right)\sqrt{w^2+x^2+d_2^2}} \right) = \\ &= \tfrac{3m\mu_0}{4\pi} \tfrac{2}{3} \left[Arc\tan\left(\tfrac{\sqrt{w^2+x^2+d_2^2}}{w} \right) - Arc\tan\left(\tfrac{\sqrt{w^2+x^2+d_1^2}}{w} \right) \right]_{x=x_1}^{x=x_2} \end{aligned}$$

concluding in:

$$B_z(x_1, x_2) = \frac{\mu_0 m}{2\pi} \left[\arctan\left(\frac{\sqrt{w^2+x^2+d_2^2}}{w} \right) - \arctan\left(\frac{\sqrt{w^2+x^2+d_1^2}}{w} \right) \right]_{x=x_1}^{x=x_2}. \tag{4.5}$$

And for a deflagration front consisting of two cuboids with opposite magnetization, with a gap of δ located at $x = x(t)$ and a total length og L, the field B_z^{total} is given by:

$$\vec{B}_z^{total} = \vec{B}_z\left(0, x(t) - \frac{\delta}{2}\right) - \vec{B}_z\left(x(t) + \frac{\delta}{2}, L\right). \tag{4.6}$$

By averaging over the size of one hall sensor and setting the experimental parameters with a constant deflagration velocity, we get peaks similar to our results as seen in Figures 4.9, 4.10 and 4.11.

In Fig. 4.12, we zoom in on the magnetization jump of a sample from the second category undergoing an avalanche at the first matching field of 0.2 T. In this figure, we show the time-resolved Hall voltage from five different sensors along the array. The three middle sensors show a peak in the Hall voltage, which is experienced by each sensor at different times. The two outer sensors experience a smoother variation of the Hall voltage, in the form of cusps, also at different times. The peaks and cusps are due to a zero magnetization front, where the magnetization **M** changes sign.

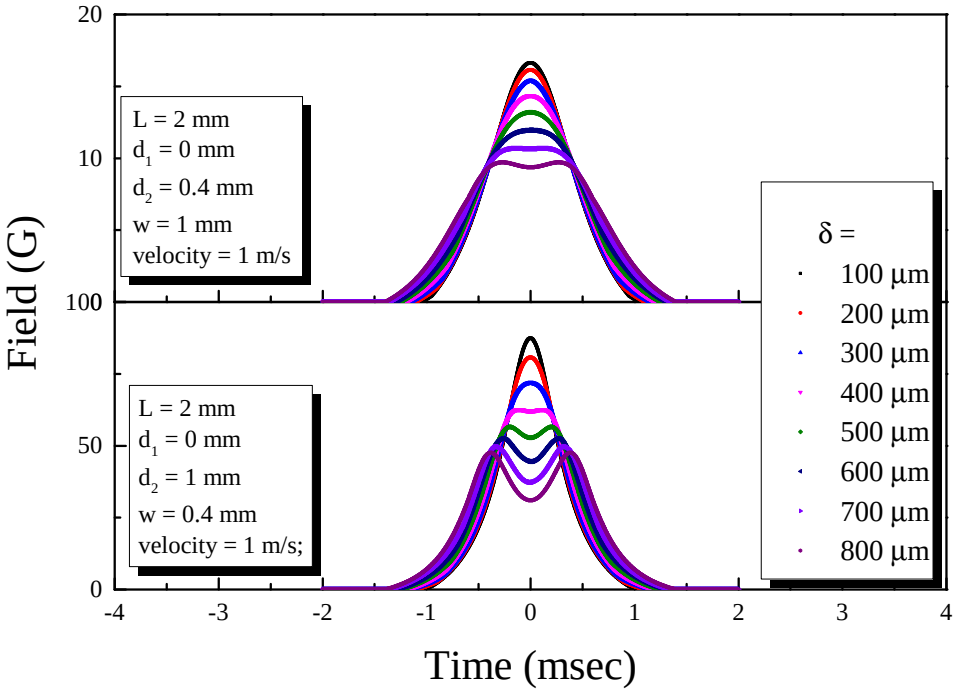

FIGURE 4.9: Calculated average field sensed by a single Hall sensor for different widths δ of the deflagration front. The top plot shows the signal from a sample sized 0.4 mm in $\hat{z}$ direction with a width of 2 mm. The bottom plot shows the signal from a sample sized 1 mm in $\hat{z}$ direction with a width of 0.8 mm. One can see that a large deflagration front width can split the peak.

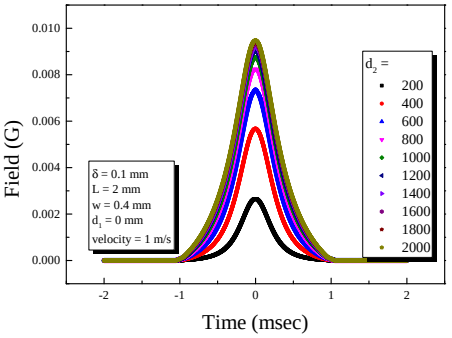

FIGURE 4.10: Calculated average field sensed by a single Hall sensor for different size $d_2 - d_1$ of the sample in $\hat{z}$ direction. One can see that increasing the size d_2 amplifies the signal.

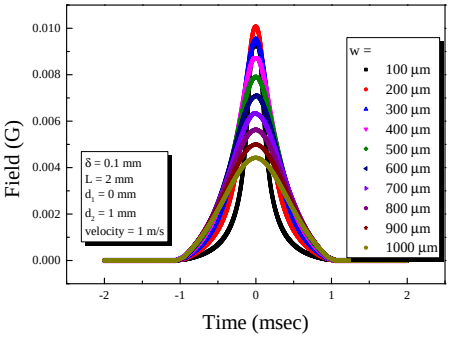

FIGURE 4.11: Calculated average field sensed by a single Hall sensor for different widths w of the deflagration front in $\hat{y}$ direction. One can see that a small width sharpens the peak.

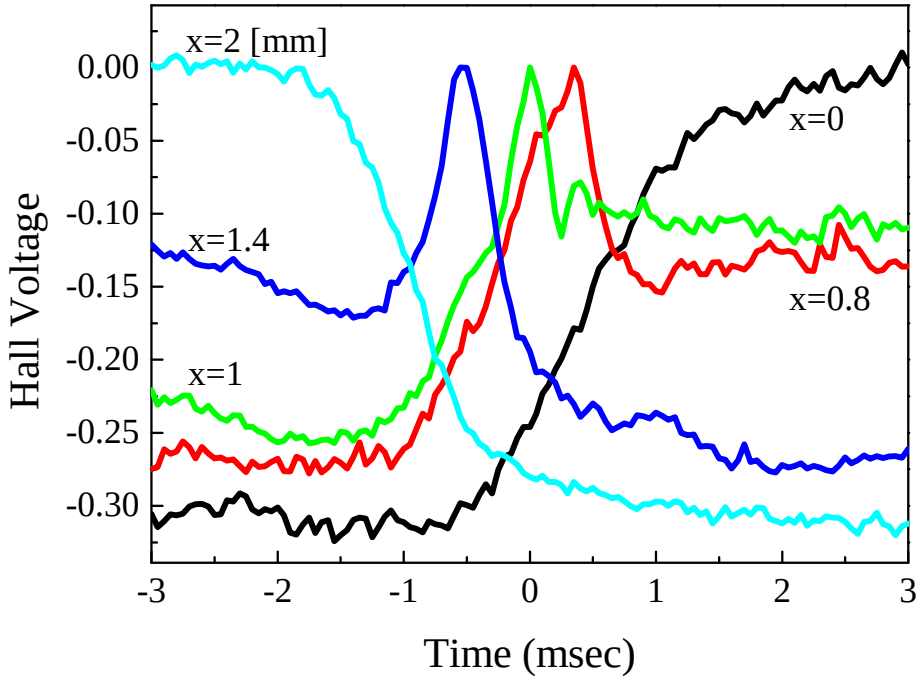

FIGURE 4.12: Hall voltage as a function of time for each of the sensors on the array for a sample that has avalanches. The voltage from each sensor shows a peak or a cusp at different times. The evolution of the peaks and cusps provides the avalanche propagation velocity.

By following the time evolution of the peaks and cusps in the Hall Voltage, we can determine the front velocity. Since the sensors are spaced apart by parts of a millimeter and the peaks are spaced apart by parts of a millisecond, the deflagration velocity V_d is of the order of 1 m/sec, which is much higher than V_m.

We found that the deflagration propagation direction and velocity can be affected by applying field gradients as long as the sweep rate is low. This is demonstrated in Fig. 4.13. In this figure, we show for each detector location, the time at which it experiences a peak or a cusp. The slope of each line is the deflagration velocity. For the lowest sweep rate of 0.83 mT/sec with no gradient, the velocity is negative. It becomes positive as the gradient is switched on to 0.14 mT/mm, but becomes slower as the gradient increases to 0.69 mT/mm. Reversal of deflagration direction, but with constant velocity magnitude, was found also in Mn_{12} by moving the sample along the main magnet axis [44]. The effect of the gradient is opposite and weaker for our highest sweep rate of 8.3 mT/sec. In this case, all velocities are positive and increase as the gradient increases. Only at the intermediate sweep rate of 1.67 mT/sec does the gradient have no effect on the velocity.

Although we found it challenging to explain the gradient dependence of the deflagration velocity, we have learned from this experiment that the safest sweep rate from which one can estimate the deflagration velocity is around 2 mT/sec. In this case, the external gradient does not affect the velocity. The ratio between sweep rates and gradient (when it is on) is a quantity with units of velocity of the order of tens of millimeters per second. This is much lower than V_d.

Therefore, for a deflagration sample, the gradient experiment is another indication that the propagation of the external magnetic field does not determine the deflagration velocity, and that V_d is an internal quantity of the molecules. In addition, a gradient-dependent V_d is not explained at present by magnetic deflagration theory.

In Fig. 4.14 we depict V_d as a function of sweep rate with zero applied gradient. The field was swept from positive to negative and vice versa. The sample used in this experiment was of the second category and produced deflagration only for sweep rates higher than 3 mT/sec. Slower sweep rates generated the usual magnetization jumps, as shown in Fig. 4.1. Although there is some difference between the velocity for different sweep directions, it is clear that the velocity tends to increase with increasing sweep rate, and perhaps saturates. This is demonstrated with raw data in the inset of Fig. 4.14. The theory of magnetic deflagration [25] does not account for sweep rate-dependent ignition, or deflagration velocities [20, 22]. In light of the gradient experiment, the most representative deflagration velocity for Fe_8 is $V_d = 0.6$ m/sec.

4.4 Thermal Diffusivity Measurement

To clarify the role of heat propagation in the deflagration process of Fe_8, we also measured the thermal diffusivity κ between 300 mK and 1 K. This was done by applying a heat pulse on one side of the sample for a duration of $\Delta t_h = 1$ msec, and measuring the time-dependent temperature on the hot side (T_{hs}) and on the cold side (T_{cs}) of a sample of length $l \simeq 1$ mm as described in section 3.8. The results are shown in Fig. 4.15. Thermal diffusivity is defined via the heat equation:

$$\frac{\partial T}{\partial t}(x,t) - \kappa \frac{\partial^2 T(x,t)}{\partial x^2} = 0 \tag{4.7}$$

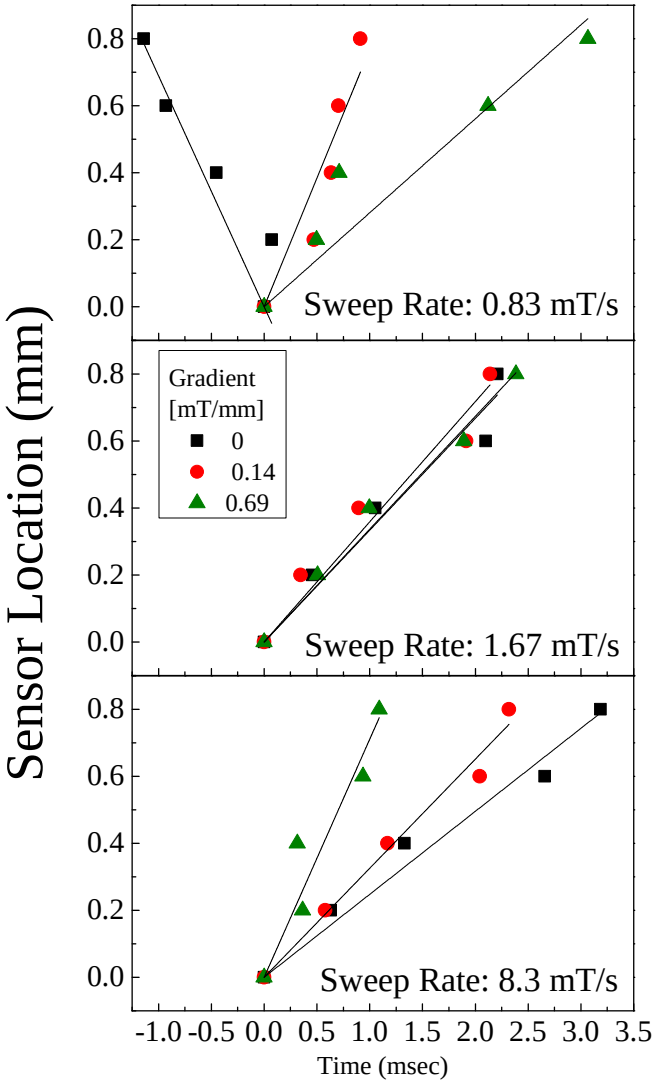

FIGURE 4.13: Sensor position as a function of time at which a peak or cusp in the Hall voltage appears for three different sweep rates and three different magnetic field gradients. The slope of each line gives the avalanche velocity.

where $T(x,t)$ is the location- and time-dependent temperature along the sample. For a long rod, where $\sqrt{\Delta t_h \kappa} \ll l$, the solution is:

$$\Delta T_{cs}(t) = c \int_0^t \frac{x \exp\left(-\frac{x^2}{4k(t-s)}\right)}{(4\pi\kappa)^{1/2}(t-s)^{3/2}} \Delta T_{hs}(s) ds. \tag{4.8}$$

We fit this expression to our $T_{cs}(t)$ data with c and κ as fit parameters. c accounts for the coupling of the two thermometers to the sample. The fit is shown by the solid line in Fig. 4.15. Although the fit is not perfect, it does capture the data quite well. The κ obtained with this method at a few different temperatures is depicted in the inset of

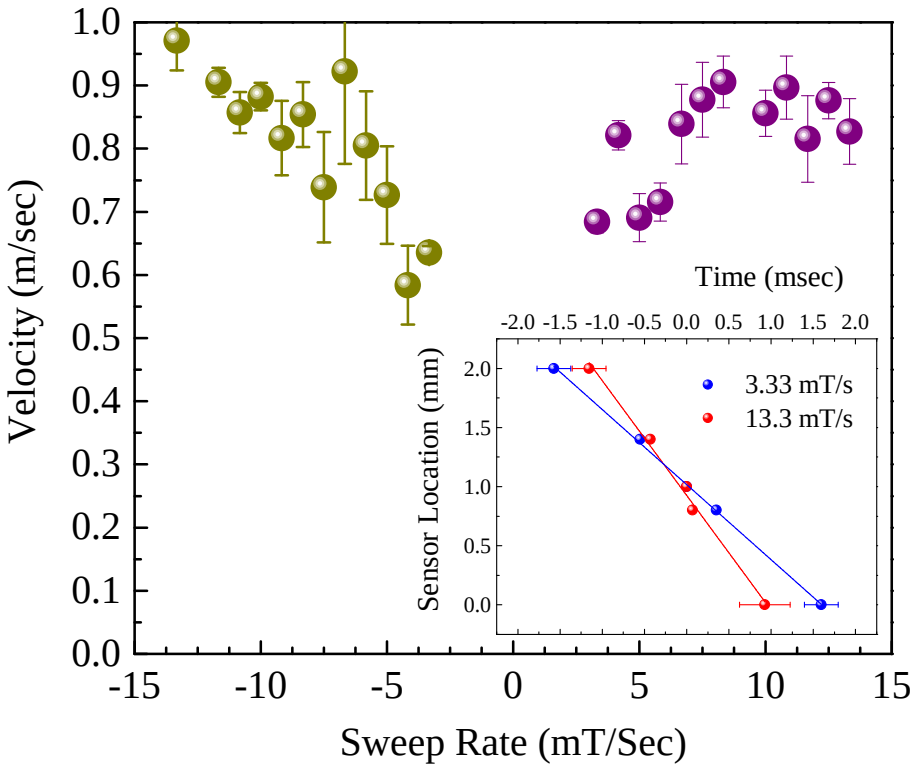

FIGURE 4.14: Avalanche velocity as a function of magnetic field sweep rate at zero gradient. The field is swept from positive to negative and vice versa. For sweep rates slower than 3 mT/sec, no avalanche was observed in this sample. The inset shows raw data of peak position vs. time for two different sweep rates.

Fig. 4.15. At the lower temperature measured $\kappa = 2 \times 10^{-6}$ m^2/sec. κ and Δt_h obey the long rod condition. It is much smaller than κ of Mn_{12}, which is estimated to be $\kappa = 10^{-5}$ to 10^{-4} m^2/sec [20, 44].

We are now in a position to estimate the flame temperature using equation 1.49:

$$V_d = \sqrt{\frac{k}{\tau_0}} \exp\left(\frac{-U}{2k_B T_f}\right).$$

We use $\tau_0 = 3.4 \times 10^{-8}$ sec and $U = 24.5$ K from Fe_8 magnetization relaxation measurements of Ref. [4]. Equation 1.49 gives $T_f = 4.8$ K. This is very similar to the energy difference between consecutive states at the bottom of the well of the Fe_8 at the first matching field, which is 4.86 K. An increase in the sample temperature during deflagration was indeed reported in Ref. [45], but with a thermometer connected to the mixing chamber. Measuring T_f properly, with a thermometer attached to the sample, could serve as a strong test of the theory of magnetic deflagration in Fe_8 molecular magnets.

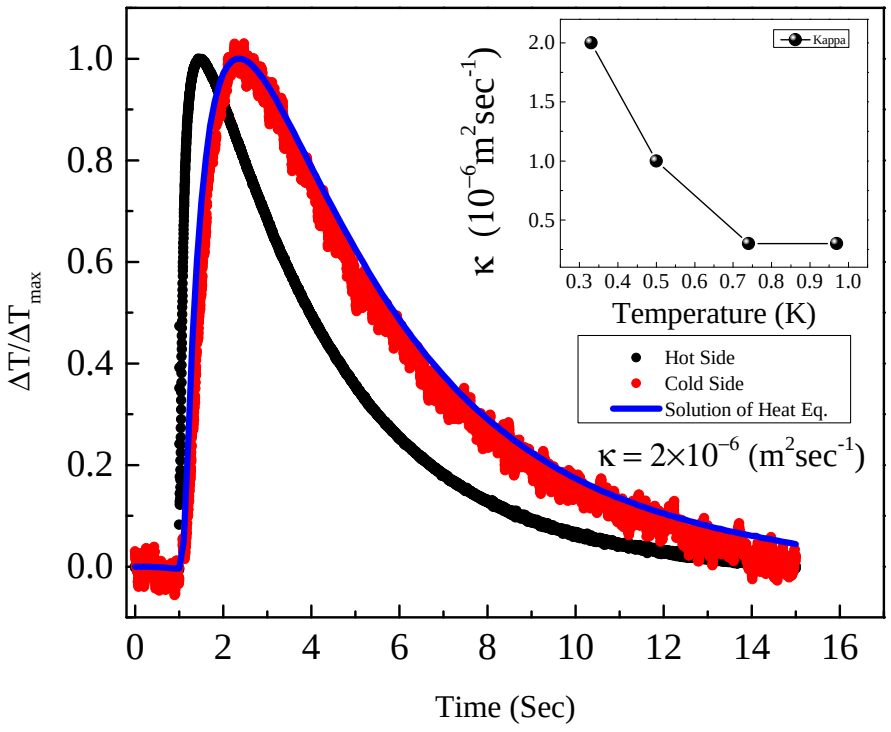

FIGURE 4.15: Normalized relative temperature as a function of time at two sides of the sample. The solid line is a solution of the heat equation for $\kappa = 2 \times 10^{-6}$. The inset shows thermal diffusivity κ at different temperatures

4.5 Summary

Contrary to a previous publication [1] we find no evidence for the release of electromagnetic radiation and place an upper limit of 5% on the total radiative energy released during the transition. The transitions between the first and second excited states to the ground state are consistent with a release of thermal energy alone. If superradiance exists in Fe_8 it is in the form of phonons rather then photons. We also observe that the energy release extends for a longer time for the second excited state than for the first excited state.

The spatially resolved magnetization measurements show that the deflagration process in Fe_8 propagates at a velocity very similar to deflagration in Mn_{12}, but has few new features: it can be ignited (in some samples) at $T \to 0$ by tunneling simply by sweeping fast through a matching field. The velocity increases with increasing sweep rate. This is surprising, since at high sweep rates fewer molecules tunnel at the ignition site, the initial flame should be colder, and the velocity slower. On the other hand, the velocity variation

could be due to increasing average field during the deflagration with increasing sweep rate. Increasing field means increasing T_f. However, within $\sim$ 1 msec of deflagration, the field changes by $\sim$ 1 mT due to the sweep, which is too small to cause noticeable variation in V_d. The velocity is also sensitive to a small gradient of $\sim$ 1 mT across the sample. This indicates extreme sensitivity to the resonance condition. It is intriguing how at a flame temperature of 5 K, when normal magnetization steps are not observed, the system is so sensitive to the sweep rate or resonance conditions.

Bibliography

[1] O. Shafir and A. Keren, "Electromagnetic radiation emanating from the molecular nanomagnet Fe_8," *Phys. Rev. B*, vol. 79, p. 180404, May 2009.

[2] S. D. Bader, "Colloquium: Opportunities in nanomagnetism," *Rev. Mod. Phys.*, vol. 78, pp. 1–15, Jan 2006.

[3] S. A. Wolf, D. D. Awschalom, R. A. Buhrman, J. M. Daughton, S. von Molnaŕ, M. L. Roukes, A. Y. Chtchelkanova, and D. M. Treger, "Spintronics: A spin-based electronics vision for the future," *Science*, vol. 294, no. 5546, pp. 1488–1495, 2001.

[4] C. Sangregorio, T. Ohm, C. Paulsen, R. Sessoli, and D. Gatteschi, "Quantum tunneling of the magnetization in an iron cluster nanomagnet," *Phys. Rev. Lett.*, vol. 78, pp. 4645–4648, Jun 1997.

[5] W. Wernsdorfer, R. Sessoli, A. Caneschi, D. Gatteschi, A. Cornia, and D. Mailly, "Landau–zener method to study quantum phase interference of Fe_8 molecular nanomagnets (invited)," *Journal of Applied Physics*, vol. 87, no. 9, pp. 5481–5486, 2000.

[6] A. Caneschi, D. Gatteschi, C. Sangregorio, R. Sessoli, L. Sorace, A. Cornia, M. Novak, C. Paulsen, and W. Wernsdorfer, "The molecular approach to nanoscale magnetism," *Journal of Magnetism and Magnetic Materials*, vol. 200, no. 13, pp. 182 – 201, 1999.

[7] R. S. Dante Gatteschi and J. Villain, *Molecular Nanomagnets*. Oxford University Press, 2006.

[8] J. R. Friedman and M. P. Sarachik, "Single-Molecule Nanomagnets," *Annual Review of Condensed Matter Physics*, vol. 1, pp. 109–128, Apr. 2010.

[9] K. Weighardt, K. Pohl, I. Jibril, and G. Huttner, "Hydrolysis products of the monomeric amine complex (c6h15n3)fecl3: The structure of the octameric

iron(iii) cation of [(C6H15N3)6Fe8(μ_3-O)2(μ_2-OH)12]Br7(H2O)br8h2o," *Angewandte Chemie International Edition in English*, vol. 23, no. 1, pp. 77–78, 1984.

[10] C. Delfs, D. Gatteschi, L. Pardi, R. Sessoli, K. Wieghardt, and D. Hanke, "Magnetic properties of an octanuclear iron(iii) cation," *Inorganic Chemistry*, vol. 32, no. 14, pp. 3099–3103, 1993.

[11] A.-L. Barra, P. Debrunner, D. Gatteschi, C. E. Schulz, and R. Sessoli, "Superparamagnetic-like behavior in an octanuclear iron cluster," *EPL (Europhysics Letters)*, vol. 35, no. 2, p. 133, 1996.

[12] Y. Pontillon, A. Caneschi, D. Gatteschi, R. Sessoli, E. Ressouche, J. Schweizer, and E. Lelievre-Berna, "Magnetization density in an iron(iii) magnetic cluster. a polarized neutron investigation," *Journal of the American Chemical Society*, vol. 121, no. 22, pp. 5342–5343, 1999.

[13] A. L. Barra, D. Gatteschi, and R. Sessoli, "High-frequency epr spectra of [fe8o2(oh)12(tacn)6]br8: A critical appraisal of the barrier for the reorientation of the magnetization in single-molecule magnets," *Chemistry A European Journal*, vol. 6, no. 9, pp. 1608–1614, 2000.

[14] R. Caciuffo, G. Amoretti, A. Murani, R. Sessoli, C. A. Caneschi, and D. Gatteschi, "Neutron spectroscopy for the magnetic anisotropy of molecular clusters," *Phys. Rev. Lett.*, vol. 81, pp. 4744–4747, Nov 1998.

[15] G. Amoretti, R. Caciuffo, J. Combet, A. Murani, and A. Caneschi, "Inelastic neutron scattering below 85 μev and zero-field splitting parameters in the Fe_8 magnetic cluster," *Phys. Rev. B*, vol. 62, pp. 3022–3024, Aug 2000.

[16] A. Mukhin, B. Gorshunov, M. Dressel, C. Sangregorio, and D. Gatteschi, "Optical spectroscopy of crystal-field transitions in the molecular magnet Fe_8," *Phys. Rev. B*, vol. 63, p. 214411, May 2001.

[17] D. Gatteschi and R. Sessoli, "Quantum tunneling of magnetization and related phenomena in molecular materials," *Angewandte Chemie International Edition*, vol. 42, no. 3, pp. 268–297, 2003.

[18] R. H. Dicke, "Coherence in spontaneous radiation processes," *Phys. Rev.*, vol. 93, p. 99, Jan 1954.

[19] C. Paulsen, J.-G. Park, B. Barbara, R. Sessoli, and A. Caneschi, "Studies of hysteresis in Mn_{12}ac," *Journal of Magnetism and Magnetic Materials*, vol. 140144, Part 3, no. 0, pp. 1891 – 1892, 1995. International Conference on Magnetism.

[20] Y. Suzuki, M. P. Sarachik, E. M. Chudnovsky, S. McHugh, R. Gonzalez-Rubio, N. Avraham, Y. Myasoedov, E. Zeldov, H. Shtrikman, N. E. Chakov, and G. Christou, "Propagation of avalanches in Mn_{12}-acetate: Magnetic deflagration," *Phys. Rev. Lett.*, vol. 95, p. 147201, Sep 2005.

[21] P. Subedi, S. Vélez, F. Macià, S. Li, M. P. Sarachik, J. Tejada, S. Mukherjee, G. Christou, and A. D. Kent, "Onset of a propagating self-sustained spin reversal front in a magnetic system," *Phys. Rev. Lett.*, vol. 110, p. 207203, May 2013.

[22] A. Hernández-Mínguez, J. M. Hernandez, F. Maciá, A. García-Santiago, J. Tejada, and P. V. Santos, "Quantum magnetic deflagration in Mn_{12} acetate," *Phys. Rev. Lett.*, vol. 95, p. 217205, Nov 2005.

[23] M. Modestov, V. Bychkov, and M. Marklund, "Ultrafast spin avalanches in crystals of nanomagnets in terms of magnetic detonation," *Phys. Rev. Lett.*, vol. 107, p. 207208, Nov 2011.

[24] W. Decelle, J. Vanacken, V. V. Moshchalkov, J. Tejada, J. M. Hernández, and F. Macià, "Propagation of magnetic avalanches in Mn_{12}ac at high field sweep rates," *Phys. Rev. Lett.*, vol. 102, p. 027203, Jan 2009.

[25] D. A. Garanin and E. M. Chudnovsky, "Theory of magnetic deflagration in crystals of molecular magnets," *Phys. Rev. B*, vol. 76, p. 054410, Aug 2007.

[26] E. del Barco, J. M. Hernandez, M. Sales, J. Tejada, H. Rakoto, J. M. Broto, and E. M. Chudnovsky, "Spin-phonon avalanches in Mn_{12} acetate," *Phys. Rev. B*, vol. 60, pp. 11898–11901, Nov 1999.

[27] D. A. Garanin and E. M. Chudnovsky, "Self-organized patterns of macroscopic quantum tunneling in molecular magnets," *Phys. Rev. Lett.*, vol. 102, p. 097206, Mar 2009.

[28] D. A. Garanin, "Fronts of spin tunneling in molecular magnets," *Phys. Rev. B*, vol. 80, p. 014406, Jul 2009.

[29] S. McHugh, R. Jaafar, M. P. Sarachik, Y. Myasoedov, A. Finkler, H. Shtrikman, E. Zeldov, R. Bagai, and G. Christou, "Effect of quantum tunneling on the ignition

and propagation of magnetic avalanches in Mn_{12} acetate," *Phys. Rev. B*, vol. 76, p. 172410, Nov 2007.

[30] S. McHugh, R. Jaafar, M. P. Sarachik, Y. Myasoedov, A. Finkler, E. Zeldov, R. Bagai, and G. Christou, "Magnetic avalanches of minor fast-relaxing species of Mn_{12} acetate," *Phys. Rev. B*, vol. 80, p. 024403, Jul 2009.

[31] S. McHugh, B. Wen, X. Ma, M. P. Sarachik, Y. Myasoedov, E. Zeldov, R. Bagai, and G. Christou, "Tuning magnetic avalanches in the molecular magnet Mn_{12}-acetate," *Phys. Rev. B*, vol. 79, p. 174413, May 2009.

[32] T. Leviant, A. Keren, E. Zeldov, and Y. Myasoedov, "Quantum ignition of deflagration in the Fe_8 molecular magnet," *Phys. Rev. B*, vol. 90, p. 134405, Oct 2014.

[33] M. Bal, J. R. Friedman, Y. Suzuki, E. M. Rumberger, D. N. Hendrickson, N. Avraham, Y. Myasoedov, H. Shtrikman, and E. Zeldov, "Non-equilibrium magnetization dynamics in the Fe_8 single-molecule magnet induced by high-intensity microwave radiation," *EPL (Europhysics Letters)*, vol. 71, no. 1, p. 110, 2005.

[34] S. Velez, J. M. Hernandez, A. Fernandez, F. Macià, C. Magen, P. A. Algarabel, J. Tejada, and E. M. Chudnovsky, "Magnetic deflagration in gd_5ge_4," *Phys. Rev. B*, vol. 81, p. 064437, Feb 2010.

[35] K. Wieghardt, K. Pohl, and W. Gebert, "[(C6H15N3)Fe2(μ-o)(μ-ch3co2)2]2+ a dinuclear iron, (iii)complex with a metazidohemerythrin-type structure," *Angewandte Chemie International Edition in English*, vol. 22, no. 9, pp. 727–727, 1983.

[36] H. London, G. R. Clarke, and E. Mendoza, "Osmotic pressure of *he*3 in liquid *he*4, with proposals for a refrigerator to work below 1 kelvin," *Phys. Rev.*, vol. 128, pp. 1992–2005, Dec 1962.

[37] N. H. Balshaw, "Practical cryogenics - an introduction to laboratory cryogenics," 1996.

[38] R. Ulrich, "Far-infrared properties of metallic mesh and its complementary structure," *Infrared Physics*, vol. 7, no. 1, pp. 37 – 55, 1967.

[39] P. A. R. Ade, G. Pisano, C. Tucker, and S. Weaver, "A review of metal mesh filters," vol. 6275, p. 62750U, SPIE, 2006.

[40] T. Timusk and P. L. Richards, "Near millimeter wave bandpass filters," *Appl. Opt.*, vol. 20, pp. 1355–1360, Apr 1981.

[41] R. Mahendiran, A. Maignan, S. Hébert, C. Martin, M. Hervieu, B. Raveau, J. F. Mitchell, and P. Schiffer, "Ultrasharp magnetization steps in perovskite manganites," *Phys. Rev. Lett.*, vol. 89, p. 286602, Dec 2002.

[42] M. Bal, J. R. Friedman, K. Mertes, W. Chen, E. M. Rumberger, D. N. Hendrickson, N. Avraham, Y. Myasoedov, H. Shtrikman, and E. Zeldov, "Experimental upper bound on superradiance emission from Mn_{12} acetate," *Phys. Rev. B*, vol. 70, p. 140403, Oct 2004.

[43] S. Bahr, K. Petukhov, V. Mosser, and W. Wernsdorfer, "Energy level lifetimes in the single-molecule magnet Fe_8: Experiments and simulations," *Phys. Rev. B*, vol. 77, p. 064404, Feb 2008.

[44] J. M. Hernández, P. V. Santos, F. Maciá, A. García-Santiago, and J. Tejada, "Acoustomagnetic pulse experiments in linbo3/mn12 hybrids," *Applied Physics Letters*, vol. 88, no. 1, pp. –, 2006.

[45] T. Leviant, S. Hanany, Y. Myasoedov, and A. Keren, "Testing the radiation emanating from the molecular nanomagnet Fe_8 during magnetization reversals," *Phys. Rev. B*, vol. 90, p. 054420, Aug 2014.

השריפה המערכת עוברת ממצב מטא-סטבילי דרך מחסום פוטנציאל למצב אנרגטי נמוך יותר. עבור אבני הדומינו המצב המטא-סטבילי הוא אבן אשר עומדת על הקצה שלה. מחסום הפוטנציאל, או במילים אחרות אנרגיית האקטיבציה - זאת האנרגיה הנדרשת על מנת להפיל אבן אחת ולגרום למפולת והמצב האנרגטי הנמוך כאשר האבן שוכבת. שוב, כמו בתהליך השריפה ישנו את האזור הקר, האזור השרוף וחזית חמה אשר מתקדמת במהירות V_d אשר קטנה יותר ממהירות הקול. החזית החמה מחממת את האזור הקר ומציתה אותו. המהירות V_d ניתנת לקירוב בצורה אנליטית על ידי פתרון של משוואת החום תחת ההנחה שהתהליך מתנהג לפי חוק ארניוס:

$$V_d = \sqrt{\frac{\kappa}{\tau_0}} \exp\left(-\frac{U}{2k_B T_f} \right)$$

כאשר κ זהו קצב הדיפוזיה של חום, τ_0 הזמן האופייני של התהליך הכימי לפי חוק ארניוס, U מחסום הפוטנציאל, k_B הוא קבוע בולצמן והגודל T_f הוא הטמפרטורה של החזית הבוערת.

בננו-מגנטים מולקולריים תהליך זה נקראה לעיתים "שריפה מגנטית". מהירות השרפה שנמדדה היא מסדר גודל של 1 מטר לשנייה כאשר הצתת השריפה מתרחשת בכל פעם בשדה הרזוננס הראשון. המהירויות שנמדדו הראו תלות בגרדיאנט ובקצב שינוי השדה החיצוני. תלות שלא טופלה כיום באופן תיאורטי.

במשוואה למהירות, הקבועים: τ_0 ו- U נמדדו בעבר והקבועים κ ו- T_f לא נמדדו. לכן על מנת שנוכל להעריך את טמפרטורת הלהבה T_f נבנה ותוכנן ניסוי אשר מדד את κ. הניסוי בוצע במקרר He^3 אשר מסוגל להגיע לטמפרטורה של 0.3Kelvin. קצב דיפוזיית החום שנמדד הוא: $\kappa \cong 2\times 10^{-6}\ \text{m}^2/\text{sec}$ וכאשר מציבים את כל המשתנים מקבלים קירוב לטמפרטורת הלהבה: $T_f \cong 4.8\text{Kelvin}$. הגודל הנראה מפתיע מכיוון שהוא גבוה יחסית לטמפרטורת המקרר.

לסיכום, נחקרה הדרך שבה נפלטת האנרגיה בזמן "איבוד הזיכרון" או היפוך המגנטיזציה של מולקולות מגנטיות. הראנו שהרוב הגדול של האנרגיה נפלט לחום והצבנו חסם עליון לקרינה אלקטרומגנטית של 5% מהאנרגיה הכוללת. נבדק תהליך של היפוך המגנטיזציה על ידי שריפה מגנטית. נמדדה מהירות התקדמות השריפה וקבוע הדיפוזיה של החום ולסיום בוצעה הערכה של טמפרטורת השריפה המגנטית.

אנרגיה זו יכולה להיפלט לקרינה או לחום בגביש. במקרה בו האנרגיה נפלת בצורת קרינה אורך הגל יהיה בקירוב 3 מ״מ. גודל הגבישים שנבדקו הוא בקירוב $3\times2\times1$ מ״מ מעוקב. כאשר אורך הגל של פליטה ספונטנית קרוב בגודלו לגודל הגביש קיימת אפשרות לנעילת פאזה בין מומנטי הדיפול של השדה החשמלי אשר תגרום להגברת העוצמה. תופעה זו דומה ללייזר, כאשר בלייזר מוגברת הפליטה המאולצת וכאן מוגברת הפליטה הספונטנית. התופעה הזו נקראת בספרות כ-Superradiance או בקצרה SR ועד כה לא נמצאו לה עדויות במצב מוצק. מחקר קודם שבוצע בקבוצה העלה השערה לקיום SR ב- Fe_8 ואפשרות זו גם נחקרה במאמר תיאורטי שחזה את התהליך. לכן המטרה הראשונה של מחקר זה הייתה לתכנן ולבצע ניסוי אשר יבדוק את קיומה של ה-SR וינסה לאפיין את אורך הגל של הקרינה.

כל המדידות בוצעות בתוך תא וואקום של מקרר מיהול (Dilution Refrigerator) אשר מסוגל להגיע לטמפרטורות נמוכות מ-0.1 Kelvin. נבנתה מערכת ניסוי המסוגלת לאפיין את כמות האנרגיה הנפלטת לקרינה יחסית לאנרגיה הנפלטת לחום. היכולת של המערכת לגלות קרינה אלקטרומגנטית נבחנה בניסוי בקרה ולאחר מספר ניסיונות רב לא נצפתה קרינה הנפלטת מהגביש בזמן דעיכה של המגנטיזציה. הוצב חסם עליון על כמות האנרגיה הנפלטת לקרינה ב-5% מהאנרגיה הכוללת המשתחררת בתהליך. התוצאות פורסמו ב- Phys.Rev.B.90,054420(2014).

המטרה השנייה של מחקר זה הייתה לחקור את האופן בו משתנה המגנטיזציה של גביש Fe_8 כתלות במקום. למטרה זו גביש של Fe_8 הודבק על פני השטח של מערך גלאים המופרדים במרחק של 0.1 מ״מ. הגלאים משתמשים באפקט הול על מנת למדוד את השדה המגנטי מעל פני השטח של הגביש בחלקים שונים. בדרך זו מתקבלת מדידת המגנטיזציה של הדגם כפונקציה של הזמן והמקום. במהלך המדידות התגלה שהיפוך המגנטיזציה, מנהור ואז דעיכה לרמת היסוד, יכולים להתרחש בשני תהליכים שונים. תהליך ראשון הוא תהליך איטי שבו המולקות מבצעות מנהור באופן בלתי תלוי במולקולות השכנות. תהליך זה מאופיין על ידי לולאת היסטרזיס בעלת מספר מדרגות רחבות בשדות החיצוניים אשר מאפשרים מנהור. תוצאות אלו תואמות למדידות קודמות אך בוצעו בטכניקה חדשה. התהליך השני נמדד לראשונה עבור חומר זה והוא מאופיין בהיפוך מהיר של כל הספינים בגביש. לולאת ההיסטרזיס, עבור תהליך זה, נראית כמו מדרגה אחת חדה של שינוי במגנטיזציה. זמן היפוך המגנטיזציה בתהליך הראשון תלוי בקצב שינוי השדה החיצוני ועבור משתני ניסוי אופייניים נמשך מספר דקות. זמן ההיפוך בתהליך השני הוא בערך מילי שניה אחת. לא יכולנו לדעת מראש איזה תהליך יתרחש בדגם מסוים והמעבר בין התהליכים קשור בעיקר לקצב פינוי החום מתוך הגביש, דבר אשר תלוי במשתנים רבים כגון: גודל וצורת הגביש, הצימוד התרמי למקרר והולכת החום. כאשר עוברים למדידה בקצב גבוה של 20 kHz מתגלה תופעה מעניינת שתהליך היפוך המגנטיזציה אינו מתרחש בכל הגביש בו-זמנית אלא מתחיל במקום מסוים ומתקדם בתור חזית בדומה לנפילה של אבני דומינו. התהליך מתחיל בדרך כלל באחד הקצוות מכיוון שהשדה המגנטי הפנימי בקצה גדול יותר. ניתן לתאר תהליך זה בפורמליזם של תהליך שריפה, בתהליך

הכולל של המולקולה מקבל ערך של $S=10$. למולקולה יש אנאיזוטרופיות מגנטית לאורך ציר מסוים. כלומר הספין יהיה מכוון לאורך ציר זה, נסמן ציר זה כ- $\hat{z}$. בטמפרטורות נמוכות, מתחת ל- 0.4 Kelvin, ניתן לכתוב את המילטוניאן הספין של מולקולה בודדת בשריג, בנוכחות שדה מגנטי חיצוני H_z בתור:

$$\mathcal{H}_0 = DS_z^2 + g\mu_B H_z S_z + \mathcal{H}_1$$

האיבר הראשון נקרא "איבר האנאיזוטרופיות" כאשר D הוא קבוע שלילי והוא גורם לספינים לבחור כיוון במרחב. איבר זה יוצר רמות אנרגיה של $m_s = m$ ו- $m_s = -m$ מנוונות עם מחסום פוטנציאל ביניהן. האיבר השני הוא איבר Zeeman הרגיל אשר גורם להעדפה של אחד מכיווני הספין והאיבר השלישי הוא האחראי על מנהור בין כיווני הספין. ניתן לתאר מערכת זו בתור בור פוטנציאל כפול כאשר בהיעדר שדה חיצוני שני הבורות בעלי עומק שווה ובהפעלת השדה אחד הבורות מעמיק בעוד השני מתרדד. במהלך הניסוי השדה נסחף מחיובי לשלילי וחוזר חלילה. במהלך הסחיפה הספינים עוברים מצד לצד בין בורות הפוטנציאל כפי שניתן לראות בתרשים הבא:

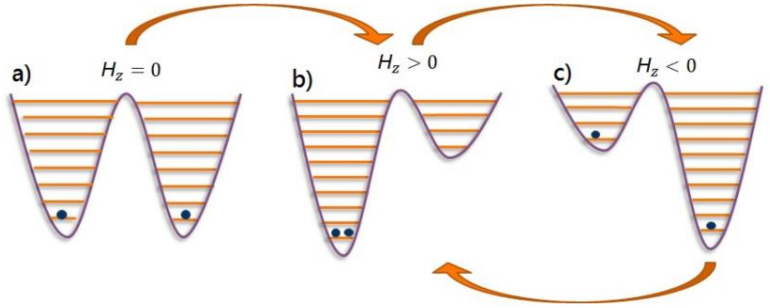

כאשר מודדים את המגנטיזציה של גביש זה כתלות בשדה החיצוני מתקבלת לולאת היסטרזיס בעלת קפיצות במגנטיזציה בשדות חיצוניים $H_m = \frac{nD}{g\mu_B}$. אלו הם ערכי שדה הגורמים למנהור בין רמות אנרגיה משני צדי הפוטנציאל. לאחר תהליך המנהור המולקולות נמצאות במצב מעורר והן דועכות לרמת היסוד. בהינתן הפרש בין רמות הספין n כאשר $\left|m_s - m_s'\right| = n$ הפרשי האנרגיה בדעיכה זו נתונים על ידי:

$$\Delta E(n) = 2n(S-n)D$$

$$\Delta E(n=1) = 5.256\,Kelvin$$

$$\Delta E(n=2) = 9.344\,Kelvin$$

תקציר

גודלן של יחידות הזיכרון הדיגיטליות עובר תהליכי מזעור במהלך העשורים האחרונים. בתחילת תקופת המחשוב השתמשו בסרטים מגנטיים, בהם יחידות הזיכרון גדולות יחסית ולכן סרטים אלו התנהגו בצורה קלאסית. יחידות הזיכרון הקלאסיות יודעות לשמור את המידע בצורה יציבה לאורך זמן בעיקר מכיוון שהן פחות מושפעות מפלקטואציות קוונטיות וכן מחסום פוטנציאל גדול בין מצבי הזיכרון. ניתן להגדיר את הגודל המינימלי עבורו היחידה תתנהג באופן קלאסי בתחום של 10^2-10^5 ספינים מגנטיים ליחידת זיכרון, גבול זה נקראה לפעמים "הגבול הקוונטי". כאשר מקטינים את יחידת הזיכרון מתחת לגבול הקוונטי תופעות קוונטיות יכולות לגרום ליחידה לאבד את המידע הרשום עליה. אחת הדוגמאות לחומרים מגנטיים מתחת לגבול הקוונטי הוא ננו-מגנטים מולקולריים. אלו הן מולקולת אורגניות המורכבות מיוני מתכת כאשר האינטראקציה בין הספינים של היונים היא פרומגנטית או אנטי-פרומגנטית. ניתן לגדל גבישים בהן המולקולות מסודרות בשריג כך שהמרחק בין המולקולות גדול יחסית לאינטראקציה המגנטית ביניהן. כאשר מקררים אותן מתחת לטמפרטורה של האינטראקציה בין היונים בתוך המולקולה, היונים קופאים כך שכל המולקולה מתנהגת כמערכת עם ספין גבוה ללא אינטראקציה עם מולקולת שכנות. אחת הבעיות ביישום מולקות אלו למטרת זיכרון היא איבוד הזיכרון בתהליכים קוונטיים כגון מנהור קוונטי. מטרת המחקר היא לחקור את תהליכי איבוד הזיכרון ותופעות נלוות כתוצאה ממנהור קוונטי. לאחר המנהור המולקולות דועכות למצב אנרגטי נמוך יותר, כתוצאה מדעיכה זו משתחררת אנרגיה אשר יכולה להשפיע על הזיכרון של מולקות שכנות. הדרך שבה אנרגיה זו משתחררת והיחסים בינה לבין שאר הגביש היא השאלה העיקרית במחקר זה.

המולקולה הנחקרת Fe_8 בעלת הרכב כימי: $[(C_6H_{15}N_3)_6Fe_8O_2(OH)_{12}]Br_7(H_2O)Br\cdot 8H_2O$ והמבנה הבא:

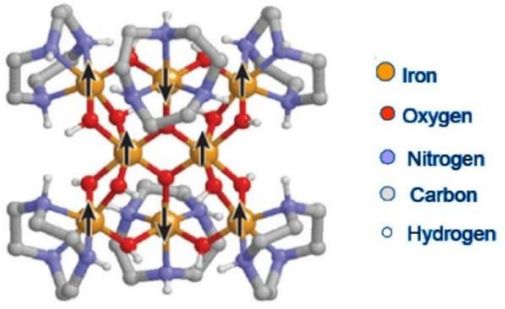

מורכבת משמונה יונים של ברזל בעלי ספין של $5/2$, כפי שניתן לראות בתרשים. בטמפרטורה נמוכה שישה יונים מכוונים לכיוון אחד בעוד השניים הנותרים מצביעים לכיוון השני כך שהספין

פרצי אנרגיה מננו-מגנט מולקולרי Fe_8 בעת מנהור קוונטי של המגנטיזציה

חיבור על מחקר

לשם מילוי חלקי של הדרישות לקבלת

התואר דוקטור לפילוסופיה

תום לויאנט

הוגש לסנט הטכניון – מכון טכנולוגי לישראל

אלול תשע"ד חיפה ספטמבר 2014

פרצי אנרגיה מננו-מגנט מולקולרי Fe_8 בעת מנהור קוונטי של המגנטיזציה

תום לויאנט